Modelling the seasonal dynamics of physical variables and the Peru- Chile Undercurrent off Central Chile (30°–40°S)

Odette A. Vergara, Vincent Echevin, Héctor H. Sepúlveda, François Colas, Renato A. Quiñones

To cite this version:

Odette A. Vergara, Vincent Echevin, Héctor H. Sepúlveda, François Colas, Renato A. Quiñones. Modelling the seasonal dynamics of physical variables and the Peru- Chile Undercurrent off Central Chile (30°–40°S). Continental Shelf Research, 2016, 123, pp.61-79. 10.1016/j.csr.2016.04.001 . hal-01298578

HAL Id: hal-01298578

https://hal.sorbonne-universite.fr/hal-01298578

Submitted on 6 Apr 2016

Modelling the seasonal dynamics of physical variables and the Peru-Chile Undercurrent off Central Chile (30°-40°S)

Odette A. Vergara[1,2], Vincent Echevín[3], Héctor H. Sepúlveda[4], Francois Colas[3], Renato A. Quiñones[1,2]

[1]Interdisciplinary Center for Aquaculture Research, Universidad de Concepción, O'Higgins 1695, Concepción, Chile

[2]Doctorate Program in Oceanography, Department of Oceanography, Universidad de Concepción, Casilla 160-C, Concepción, Chile

[3]Laboratoire d' Oceanographie et de Climatologie: Expérimentation et Analyse Numérique (LOCEAN), Institute Pierre-Simon Laplace (IPSL), UPMC/CNRS/IRD/MNHN, 4 Place Jussieu, Case 100, 75252 Paris cedex 05, France

[4]Department of Geophysics, University of Concepción, Concepción, Chile

Abstract

The seasonal variability of the hydrology and the poleward subsurface Peru-Chile Undercurrent (PCUC) off the central Chilean coast (29°-41°S) were examined using a high-resolution regional model. The model realistically reproduced observed sea level variability, such as intense anticyclonic eddies, the offshore intensification of the poleward flow and the reduced nearshore equatorward flow during autumn, as well as the equatorward intensification of nearshore meandering flow during spring. Values for geostrophic eddy kinetic energy were high along the coast between 30° and 37°S, and lower south of this area. The modelled poleward undercurrent showed latitudinal variability in velocity and transport. The maximum average transport reported was 0.8 Sv near 30°S, consistent with previous modelling studies and estimations derived from *in situ* observations. The poleward reduction in undercurrent strength was shown to be partly generated by the poleward decrease in wind stress curl and by the formation of a westward jet near 35°S associated with westward-propagating eddies. A Lagrangian analysis of the modelled water parcels transported by the undercurrent shows that only 14-20% of the subsurface floats transported by the undercurrent upwelled into the surface layer within the subsequent six months after their release. The floats remaining within the subsurface layer were likely transported further south by the current, offshore by westward-propagating eddies or equatorward by the deeper part of the surface coastal current.

Abbreviations

AAIW, Antarctic Intermediate Water; AVHRR, Advanced Very High Resolution Radiometer; AVISO, Archiving, Validation and Interpretation of Satellite Oceanographic data; CARS, CSIRO Atlas of Regional Seas; CCC, Chile Coastal Current; COADS, Comprehensive Ocean-Atmosphere Data Set; CSIRO, Commonwealth Scientific and Industrial Research Organisation; CTW, coastal trapped waves; EBUS, Eastern Boundary Upwelling Systems; EKE, Eddy Kinetic Energy; ESSW, Equatorial Subsurface Water; ETOPO2, Earth Topography and Bathymetry; EUC, Equatorial Undercurrent; HCS, Humboldt Current System; FIP, Fondo de Investigación Pesquera y Acuicultura; IEKW, intraseasonal equatorial Kelvin waves; KPP, K-Profile Parameterization; PCCC, Peru-Chile Countercurrent; PCUC, Peru-Chile Undercurrent; PDW, Pacific Deep Water; POM, Princeton Ocean Model; ROMS-AGRIF, Regional Oceanic Modeling System - Adaptive Grid Refinement in FORTRAN; SAAW, Sub-Antarctic Water; SCOW, Scatterometer Climatology of Ocean Winds; SLA, Sea Level Anomaly; SSCC, Southern Subsurface Countercurrent; SST, Satellite Sea Surface Temperature; STW, Subtropical Water.

Keywords: Ocean modelling; poleward subsurface Peru-Chile Undercurrent; Eastern Boundary Upwelling System; Humboldt Current System.

1. Introduction

The Eastern Boundary Upwelling (EBUS), California, Humboldt, Canarias and Benguela systems, are among the most productive marine systems in the world and support the greatest pelagic fisheries on earth (Chávez et al., 2003; Chávez et al., 2008; Pauly and Christensen, 1995). In these regions the wind is generally parallel to the coastline and forces a nearshore upwelling, which brings cold, nutrient-replete deep water to the surface, generating high levels of biological productivity. Understanding the dynamics of the EBUS is highly relevant given the local manifestations of climate change, such as ocean acidification (Gruber et al., 2012) and wind regime change (Bakun, 1990, Bakun et al., 2010, Belmadani et al., 2014, Garreaud and Falvey, 2009, Sydeman et al., 2014). Changes in winds due to increased greenhouse gases could modify upwelling, which together with changes in the characteristics of water masses (e.g. subsurface nutrient concentration), could significantly affect coastal ecosystems (Aiken et al., 2011, Brochier et al., 2013, Gutierrez et al., 2011, Oerder et al., 2015).

The Humboldt Current System (HCS) is part of the general circulation of the Southeastern Pacific Subtropical Gyre and contains complex movements of surface waters towards the equator and the pole (Schneider et al., 2004). Off Central Chile (30°-40°S), the flow of oceanic and coastal branches of the HCS driven by the meridional winds associated with the South Pacific anticyclone intensify during summer and diminish during winter (Fuenzalida et al., 2008). The HCS is composed of several currents: the surface Chile Coastal Current (CCC) above a depth of 100 m between the continental shelf and the slope flowing towards the equator during summer; the poleward surface Peru-Chile Countercurrent (PCCC), which flows between 100 and 300 km offshore above a depth of 100 m, reaching maximum velocities in spring and minimum velocities in autumn (Strub et al., 1995, 1998); and the poleward subsurface Peru-Chile Undercurrent (PCUC), which flows below the CCC between 100 and 400 m (Strub et al., 1998). The northern and central coast of Chile (18° to 38°S), where the PCUC dominates, is highly productive in terms of fisheries. Sardine and anchovy are among the most abundant resources in the first 100 nm from the coast (Cubillos et al., 2002, 2007; Cubillos and Arancibia, 1993). These important biological resources are generated by the combination of upwelling and the fuelling of nutrients by the PCUC (Fonseca, 1989; Quiñones et al., 2010).

Poleward subsurface currents such as the PCUC are present in every EBUS (Fonseca, 1989, Hill et al., 1998; Neshyba et al., 1989) at mid-latitudes, opposing the equatorward surface flow (Pierce et al., 2000). These subsurface currents generally reach average velocities along the coast of ~0.05 m/s to ~ 0.2 m/s, distributed between depths of 150 and 300 m, as reported for the California Undercurrent (e.g. Gay and Chereskin, 2009; Hickey, 1979; Thomson and Krassovski, 2010) and the Iberian Peninsula (0.2 m/s; Haynes and Barton, 1990; Torres and Barton, 2006). In the HCS, the PCUC originates off the coast of Peru near 5ºS and flows as far south as the Gulf of Penas (48ºS; Silva and Neshyba, 1979; Wooster and Gilmartin, 1961; Wooster and Reid, 1963). The origin of the PCUC is generally recognized as stemming from the EUC (Equatorial Undercurrent) and two branches of the SSCC (Southern Subsurface Countercurrent; Montes et al. 2010, Czeschel et al. 2011).

Direct measurements of the PCUC have been made off the coast of Peru (Chaigneau et al., 2013; Huyer et al., 1987) and Chile (Codispoti et al., 1989; Pizarro et al., 2002; Shaffer et al., 1997, 1999). Based on 6 years of data at 30ºS, Shaffer et al. (1999) reported an average velocity of 12.8 cm/s at 220 m, with semiannual variation and an intensified poleward flow in spring. The average estimated transport of the PCUC at 30°S is 1-1.3 Sv (Huyer et al., 1987; Shaffer et al., 1999, 2004).

The semi-annual variations of the PCUC are responses to the combination of local wind stress curl and disturbances caused by remote tropical forcing (Pizarro et al., 2002; Ramos et al., 2006). This flow is also modulated interannually by Rossby waves forced by trapped waves propagating southward along the coast of South America (Belmadani et al., 2012; Pizarro et al. 2002), a physical mechanism that also partly explains the variability in the oxygen minimum zone off Chile (Hormazábal et al., 2006).

The PCUC is thought to be fuelled by Equatorial Subsurface Water (ESSW) as a consequence of periods of intense and persistent wind-driven upwelling in southern-central Chile, leading to low oxygen conditions (Fuenzalida et al., 2009; Hernández-Miranda et al., 2010; Ulloa and Pantoja, 2009) and high nutrient concentrations, which favour primary productivity (average annual of 10-20 g C.m-^{2}.day^{-1}, Daneri et al., 2000; Montero et al., 2007). The ESSW is located below the subtropical water mass (STW) off Peru (10-18ºS) and above Subantarctic Water (SAAW) off Chile (25-48ºS; Silva et al., 2009). Originally described by Gunther (1936), this water mass is characterized by a subsurface salinity maximum (~34.9) and by low dissolved oxygen concentrations (4.4-44.6 µM, 2-15% saturation) and high nutrient concentrations (20-40 µM nitrate, 2.6-3 µM phosphate; 25-40 µM silicate; Silva et al., 2009). The PCUC transports this water mass along the continental slope off Peru and Chile (Silva and Fonseca, 1983; Strub et al., 1998; Wooster and Gilmartin, 1961; Wyrtki, 1967), until it disappears near 48ºS (Silva and Neshyba, 1979).

Given the influence of the PCUC on the poleward transport of the ESSW, studying its dynamics on the continental slope along the coast of Chile is relevant to understand north-south nutrient, oxygen and plankton fluxes, which play an important role in sustaining high biological productivity in the HCS. Numerical modelling is a very useful approach to understand the characteristics and dynamics of currents. Several modelling studies have been conducted in the Chile region. Using a high-resolution model, Batteen et al. (1995) studied the response of the Chile coastal region from 22.5°S to 35°S to climatological wind forcing. They showed that equatorward winds generate mesoscale features and a poleward flow of 5 to 15 cm/s. Other works have employed the Princeton Ocean Model (POM, Blumberg and Mellor, 1987). Mesias et al. (2001) characterized circulation in the Gulf of Arauco (37°S) during summer and the effect of seafloor topography and coastal geometry on the upwelling regime, highlighting the formation of an equatorward coastal jet during the active upwelling phase. Leth and Shaffer (2001) used POM to study circulation off central Chile, reproducing an equatorward coastal current, a poleward undercurrent and the formation of meanders and eddies in response to the baroclinic instability of the flow. Leth and Middleton (2004) found that the presence of a cyclonic gyre in conjunction with the upwelling-favourable wind enhanced upwelling in the Gulf of Arauco. More recently, the Regional Ocean Modeling System (ROMS, Shchepetkin and McWilliams, 2005, see section 2.a) has been applied to upwelling regions in the southeast Pacific, analysing circulation and seasonal (Aguirre et al., 2012; Penven et al. 2005), interannual (e.g. the 1997-1998 El Niño event, Colas et al., 2008) and intraseasonal variability (Belmadani et al., 2012; Echevin et al., 2014). Process studies have also addressed the impact of mesoscale eddies on heat balance (Colas et al., 2012), ocean surface dynamics (Aguirre et al., 2012, 2014) and their impact on larval transport (Parada et al. 2012; Soto et al., 2012; Yanicelli et al., 2012). However, none of the previous studies have focused in detail on the seasonal dynamics of the PCUC along the Chilean coast and their influence on the poleward transport of water masses.

The objectives of the present study are to: (a) characterize the nearshore dynamics of the HCS in central Chile (30-40ºS, 70º-80ºW) using a high-resolution regional model and to determine the seasonal variability of physical variables (temperature, salinity, density and sea surface height); (b) describe the seasonal variability of the PCUC in terms of transport and velocity along the Chilean coast; and (c) study the trajectory of water masses using Lagrangian float diagnostics. In this study, we focus on the nearshore zone, which corresponds a ~100-200 km-wide coastal band as opposed to the open ocean off the continental margin. The methodology is described in Section 2. The hydrodynamic model configuration is presented in section 2.1, and the diagnostics for the PCUC characteristics and for the Lagrangian analysis of water masses transported by the PCUC are described in Sections 2.2 and 2.3, respectively. The water masses are described in Section 2.4 and the data used to assess the realism of the model are presented in Section 2.5. The results on the mean and seasonal cycle of the main physical variables of the model are presented in Section 3.1, while Section 3.2 presents the results of the Lagrangian analysis. The discussion is presented in Section 4 and the conclusions are summarized in Section 5.

2. Methods

2.1. Hydrodynamic model and grid configuration

The hydrodynamic model used in this study is the ROMS-AGRIF (Regional Oceanic Modeling System - Adaptive Grid Refinement in FORTRAN, Schepetkin and McWilliams, 2005, Penven et al. 2006; http://www.romsagrif.org). This model utilizes sigma (terrain-following) coordinates in the vertical plane and orthogonal-curvilinear coordinates in the horizontal plane. It solves the primitive hydrostatic equations with an explicit free-surface scheme. Subgrid-scale vertical mixing is parameterized using the KPP (K-Profile Parameterization) boundary layer scheme (Large et al., 1994). Bottom topography from the SRTM30 database (Becker et al., 2009) was interpolated onto the model grid and smoothed following Penven et al. (2005) to reduce pressure gradient errors. Simulations were carried out on a grid between 29°S and 41°S, and from 69°W to 83°W (Fig. 1), with a resolution of 7.5 km and 32 sigma levels. The initial and open boundary fields were obtained from a monthly climatology of a simulation analysed by Colas et al. (2012; Peru-Chile Model, with a spatial resolution of 7.5 km and 32 vertical sigma levels) using the “Roms2Roms” offline interpolation package (Mason et al., 2010). Open boundary conditions were treated using an Orlanski scheme for the tracers and baroclinic velocities, and a Flather scheme for the barotropic mode (Marchesiello et al., 2001).

The atmospheric forcings used were the 0.25°x0.25° SCOW wind stress (Scatterometer Climatology of Ocean Winds, Risien and Chelton, 2008, Fig. 2) derived from Quikscat data and heat and fresh water fluxes from COADS climatology (Comprehensive Ocean-Atmosphere Data Set, da Silva et al., 1994). A relaxation of the modelled sea surface temperature to the Pathfinder monthly climatology (Casey et al. 2010) was imposed following the parameterization of Barnier et al. (1995) with a nudging coefficient with slight spatial and temporal variations, between ~-25 and ~33 W m^{-2} $°C^{-1}$. A relaxation to COADS surface salinity with a time scale of 30 days was also included, whereas the runoffs of Chilean rivers (e.g. The Biobio River near 36°S) were not explicitly incorporated into the simulation.

Ten years were simulated, of which 9 were used to obtain an average climatological year of physical variables (temperature, salinity, currents and sea level) and to do the Lagrangian analysis. Seasonal means correspond to JFM (summer), AMJ (autumn), JAS (winter), and OND (spring).

2.2. Currents

2.2.1. Transport along the coast

Average monthly and seasonal transports were calculated at 30ºS, 33ºS, 36ºS and 39ºS to determine the spatial and temporal variability of the PCUC along the continental slope in the study area. For each month of model output, velocity fields were interpolated from sigma levels to z levels every 5 meters. Then, negative (poleward) velocities between the surface and a maximum depth of 650 m and between the coast and 100 km offshore were integrated to compute poleward transport. The modelled transport was also compared to that obtained in other studies (Leth et al., 2004; Pizarro et al., 2002; Shaffer et al., 1997,1999), and in previous model simulations (Aguirre et al., 2012; see Table I).

2.2.2. Longitudinal width and nucleus of maximum PCUC velocity

The average east-west (zonal) width of the poleward current (defined as negative velocity) and the maximum velocity at a depth of 200 m (which corresponds to the average shelf break depth between 30°S and 40°S) were determined seasonally (autumn, winter, spring, summer) at 30°, 33°, 36° and 39° S.

2.3. Trajectory of the water masses transported by the PCUC

The ROMS- offline tracking module was used to calculate numerical Lagrangian trajectories of water parcels from three-dimensional ROMS velocity fields (Capet et al., 2004; Carr et al., 2008). This type of numerical method has proved to be appropriate for studying the origin and the trajectory of ocean water masses (Blanke et al., 2002; Mason et al., 2012; Montes et al. 2010). Virtual Lagrangian floats were launched in the PCUC core along two cross-shore sections (33° and 37°S) with a vertical spacing of 15m in the vertical and 2km in the horizontal. For each month of the 9-year-long simulation, approximately 800 floats were initially released along the sections in the PCUC at depths between 50 m and 700 m, and within 200 km from the coast,. Their trajectories were then integrated for a period of six months, with a time step of 14.4 minutes and using model outputs every 3 days. Statistics on the trajectories of the floats originating from the PCUC were computed. Floats were considered to be upwelled when they reached the surface layer delimited by a depth of 50m. We then computed the initial depth of the “upwelled” floats within the PCUC sections and the transit time of the floats between their initial and final position (i.e. where they entered the surface layer) (see Table II). Statistics were compiled for the floats that were not upwelled in their 6-month transit: the distance to the coast, latitude and initial depth of the floats (see Table III).

2.4. Water masses

Using the ROMS data, a temperature-salinity (TS) diagram was plotted for the region [35.5º-40°S;

72.75º-77.8°W] to determine the water masses present in the study area during the summer season. The water masses from this study area (Bernal et al., 1982; Silva et al., 2009; Silva and Konow, 1975) are characterized as follows: Subtropical Water (STW), >18.5 °C >34.9, Subantarctic Water (SAAW), 11.5-14.5 °C, 34.1-34.8, Equatorial Subsurface Water (ESSW), 8.5-10.5°C, 34.4-34.9 Antarctic Intermediate Water (AAIW), 4-8 °C, 34.3-34.5 and Pacific Deep Water (PDW), 1.75 °C, 34.68 .

Additionally, the composition of each water mass (percentage) at 37°S; 75.3°W (Gulf of Arauco) in the vertical profile of salinity and temperature during summer was calculated. The percentage of water types was calculated by the mixing triangle method (Silva and Konow, 1975), using the values indicated by Silva and Konow (1975) and Silva et al. (2009). This latitude was chosen because of the enhanced upwelling in the Gulf of Arauco (Leth and Middleton, 2004).

2.5. General assessment of the simulation

2.5.1 Sea level height and eddy kinetic energy

AVISO (Archiving, Validation and Interpretation of Satellite Oceanographic data) satellite altimetry data was used for 1992–2005 to assess the variability of the modelled sea level height (http://www.aviso.oceanobs.com/). With these data the sea level anomalies for autumn and spring in the study area were calculated. The average geostrophic eddy kinetic energy (EKE), a measure of surface mesoscale turbulence, was computed from the surface geostrophic current anomalies derived from the sea level anomalies. The same calculation was made using the model output.

2.5.2. Temperature and salinity

Satellite Sea Surface Temperature (SST) from the Advanced Very High Resolution Radiometer (AVHRR) Pathfinder product version 5.0 (Casey et al. 2010) was compared to simulated SST. In addition, cross-sections of average ROMS temperature and salinity at 32° and 36°S were compared to observations from the CSIRO Atlas of Regional Seas (CARS2006; Dunn and Ridway, 2002; Ridway et al., 2002) climatological database.

Hydrographic data from three summer cruises at 35.5º-40°S; 72.75º-77.8°W carried out by the Chilean Fund for Fisheries and Aquaculture Research (Fondo de Investigación Pesquera y Acuicultura, Ministry of Economy, Chile: FIP, www.fip.cl) were used to observe the presence of water masses using TS diagrams and to determine the percentage of each water mass between 0 and 700 m depth (REF). These cruises were carried out in December 2005 (FIP 2005-01), January

2009 (FIP 2008-20) and January 2011 (Fip 2009-39). The TS diagram and percentage of water masses from the FIP cruises were compared to the ROMS simulation.

3. Results

3.1. Average fields and seasonal variability

3.1.1. Sea level variability

The seasonal climatology of the modelled sea level anomaly (SLA) was compared to the climatology of AVISO for the period 1992-2005 (Fig. 3). The simulated and observed SLA anomalies were consistent in magnitude and their patterns were qualitatively similar. The spatial correlations and standard deviations are compared in a Taylor diagram (Fig. 3e). The correlations vary between 0.4 (spring), 0.5 (summer) and 0.6 (autumn and winter). Standard deviations are between 40% (spring) and 70% (winter) higher in the model than in the observations, suggesting that the modelled mesoscale activity is slightly overestimated.

The most significant seasonal changes occur in a 300-km-wide coastal band, from ~73°- 76°W. The gradients of SLA indicate the presence of anomalous surface geostrophic currents, tangential to the isolines, and not the total geostrophic current. Positive SLA dominated near the coast in autumn (Fig.3 a,b), with relatively higher values (1-3 cm) in the model. The presence of relatively intense anticyclonic mesoscale eddies in the model associated with positives anomalies, can be noted both offshore (near 33°S-80°W and 39°S-79°W in autumn, Fig. 3a) and nearshore (within 2° from the coast, Fig. 3a). The nearshore anticyclonic structure (32°S-73°W, see label A1 in Fig. 3a) was also found nearly at the same location in longer model simulations (e.g. 20 years, Figure not shown), which suggests that this eddy is triggered seasonally in autumn at this location. The negative SLA along the coast (<-2 cm) in spring (Fig. 3d) indicates an intensification of the equatorward geostrophic meandering flow (Fig.3f), while positive offshore values (1-2 cm) suggest the presence of a strong poleward meandering flow between 78°W-76°W. Overall, the meridional, alongshore-averaged, surface geostrophic current is equatorward nearshore and intensifies in spring and summer (Fig.3f).

The modelled geostrophic EKE was compared to the geostrophic EKE derived from AVISO data, with relatively good agreement ($r=0.7768$, $p<0.05$) as both the modelled and observed patterns of EKE displayed high values (>120 cm^2s^{-2}) in a offshore strip between 30° and 37°S, and lower values south of this area (Fig. 4). As in other upwelling systems, there was an EKE nearshore minimum in both the simulation and the observations, supporting the idea that the EKE originate from instabilities in the nearshore region that amplify while moving offshore (Marchesiello et al., 2003). Note that the modelled EKE was nevertheless higher than the observed between 30° and 38°S in a 200-300-km wide coastal band, which indicates that the modelled current system tends to be more unstable than the real one. These discrepancies may also be partly due to lower quality data for nearshore regions (Capet et al., 2014).

3.1.2. Temperature and salinity

The average SST model oscillated between 11° and 18°C and displayed minimum values near the coast as expected from coastal upwelling. It compared well with Pathfinder data, with differences of less than ~1 °C (Fig. 5a).

The SST Hovmöller computed in a coastal band (Fig. 5b) revealed good agreement between the modelled SST and the data, especially from April to December (autumn, winter and spring season). An exception was observed during summer months (January to March) in the north of the study area (30º-33ºS) where Pathfinder data revealed a maximum of 20°C, differing from the ROMS simulation with a maximum of 18°C.

Yearly averages of simulated temperature cross-sections at 33° and 36°S compared well to observed values (Fig. 6). At 33°S between 0 and 200 m the model simulated a temperature between 10.5º and 17ºC (Fig. 6a), while CARS data revealed slightly lower temperatures of 10°-15 °C (Fig. 6b). At 36°S between 0 and 200 m, temperatures were between 10.5º and 16 °C in the model (Fig. 6c) and between 10° and 15°C in CARS data (Fig. 6d). The model and observed isotherm shoaling toward the shore both indicate coastal upwelling. The thermal stratification over the top 100 m is relatively similar in the model and observations, although the thermocline seems more pronounced in CARS. However, the model did not realistically represent the weakly stratified layer near the coast, located between the surface and a depth of ~200 m, at 36°S (Fig. 6d). The resolution of the CARS gridded product is limited to 50 km, which could explain some of the discrepancies between the observations and the model fields.

Maximum salinity was located near the coast, at slightly greater depths (~200-400 m, S~34.52, Figs. 6) in the model than in CARS (~150-300m, S~34.64, Figs. 6 f,h). Maximum salinity was found at a depth of approximately 250 m, which corresponds closely to the subsurface salinity maximum associated with the PCUC, with a lower value in the model than in the data. Colas et al. (2012) found the same bias in the value of the maximum salinity in their simulation of the HCS, which was used as boundary conditions for our model. The salinity maximum diminishes poleward, with a ~0.04 decrease between 33° and 36°S in the model and in the observations.

3.1.3. Density and water masses

Both the model and observed density values from FIP summer cruises (January, February, March) at 35.5º-40°S; 72.75º-77.8°W, are between 27.5 kg m^{-3} for deep waters and 24.5 kg m^{-3} for surface waters (Fig. 7a,b). However, the FIP data at the surface reached salinities close to 33 while simulated values were no lower than 34. The salinity range for densities between 24.5-26.5 is also much lower in the model (33.7-34.4) than in the FIP data (33.3-34.6). The modelled WM characteristics are consistent with those imposed at the northern and southern boundary of the model (Figure 7c,d). They are particularly similar to the T/S characteristics from the northern boundary (Fig.7c), which suggests that the nearshore WMs are mainly of northern origin, transported poleward by the PCUC and upwelled. The low salinity (33.3-33.7) surface waters encountered at the southern boundary (41°S, Fig. 7d) are likely mixed with more saline surrounding waters before they reach the FIP cruise sites.

The simulated and observed water masses in summer at 37ºS; 75.3ºW were: STW, SAAW, ESSW, AAIW and PDW (Fig. 7e). Several discrepancies were observed in the percentages of some of the water masses in the water column between 0 and 700 m. STW in the data and the simulation amounted to up to 10% at 100 m, while SAAW was apparent between 80 and 300 m, representing 80% in the simulation and almost 90% in the FIP data. Greater differences were observed for ESSW, which displayed a high percentage (55%) at 300 m in the simulation and a higher value (70%) at 250 m in the data. AAIW represented a high percentage at 350 m (45%) in the simulation and at 400 m (45%) in the data (Fig. 7e).

3.1.4. Currents

Meridional cross-sections were taken at 30º, 33º, 36º and 39°S to observe the location of the PCUC nucleus, width and depth and to determine latitudinal gradients in the simulated alongshore currents (Fig. 8). The mean current displayed significant changes between 30° and 39°S. At 30°S the mean flow displayed a well-marked PCUC at depths between ~100 and 600m (Fig. 8a) trapped along the continental slope, with a shallow maximum trapped along the coast at depths between 50 and 200 m. Above the PCUC, the equatorward CCC was linked to a quasi-barotropic offshore equatorward flow, particularly marked in autumn and winter (Fig. 8a). Near 33°S the PCUC had a subsurface maximum trapped on the slope near ~200-300 m depth. It was linked to an offshore surfacing poleward flow, likely the PCCC (Strub et al., 1995), located between 50 and 100 km from the coast and particularly intense in spring and summer (Fig. 8b). Both the PCUC and PCCC weakened further south. Near 36°S there was no clear evidence of a coastally-trapped PCUC, and the offshore poleward flow associated with the PCCC had also weakened (Fig. 8c). At 39°S (Fig. 8d) both the cores of the PCUC and PCCC reappeared near the slope (mainly in summer) and ~100-120 km from the coast (mainly in winter), respectively. Their intensities were weaker than near 30° and 33°S. At the coast, the surface equatorward CCC strengthened and thickened at 39°S in comparison to further north. Differences in position, width, and strength of the HCS can partly be explained by the region's wind stress pattern (Fig. 9). There are seasonal differences in wind stress, mainly between winter and summer (Fig. 9c), which creates a distinct wind stress curl pattern for the two seasons (Fig. 9d). Nearshore negative wind stress curl was found along the four sections (Fig. 9b), except over a narrow band along the coast at 36° and 39°S. As negative nearshore wind stress curl drives a poleward transport according to the Sverdrup relation (Sverdrup, 1947), the poleward increase of wind stress curl (Fig. 9b) may partly drive the poleward decrease in PCUC intensity (see also Fig. 10). The surfacing poleward flow (PCCC) detected at 33ºS (Fig. 8b) and 39ºS (Fig. 8d) resembles the outcropping of the modelled PCUC off Peru (Penven et al., 1995), which may reach the surface in the case of cyclonic stress curl (McCreary and Chao, 1985). The reduction in PCUC intensity near 35°S (Fig. 8b-c and 10a) might also be related to the formation of a westward subsurface jet near 35°S, associated with westward-propagating eddies (Fig. 10b).

The east-west width and depth of the maximum velocity nucleus of the PCUC varied seasonally and latitudinally (Fig. 11). At 30°S the current was located near the shelf with no major seasonal changes in width and cross-shore position of maximum velocity. The PCUC at this latitude reached a width of ~50 km and the maximum velocity nucleus was located 20 km from the shelf. The depth of the nucleus was found at 100 m in autumn, spring and summer, and 150 m in winter

(Fig. 11). This weak seasonality at 30ºS could be related to the narrow continental shelf and the year-round upwelling-favourable winds. At 33°S, there was greater seasonal variability; during autumn and winter the average width was 50 km, centred on the nucleus of maximum velocity at approximately 30 km from the shelf (Fig. 11). In depth there were also marked seasonal differences; the maximum velocity nucleus was located at a depth of 200 m in autumn and summer, at 250 m in winter and at 230 m in spring (Fig. 11).

At 36°S the PCUC was often composed of two cores of poleward velocity (Figure 8c). We computed the total width of the poleward flow, i.e. the sum of the widths of the two branches. During winter and spring the average width was approximately 110 km, and the nucleus of maximum velocity was located in the offshore current vein at 80 km from the shelf (Fig. 11). In autumn the average width of the current was 130 km, with a nucleus 60 km from the shelf (Fig. 11). During summer the PCUC was on average 120 km wide, with a maximum velocity nucleus at 60 km from the shelf (Fig. 11). In winter and summer the maximum velocity was registered at a depth of 250 m; at 200 m in autumn and at 225 m in spring (Fig. 11). At 39°S, the current was weaker (Fig.8d) and narrower than at other latitudes. In autumn and winter the average east-west width was 30 km, with a maximum velocity at approximately 20 km from the shelf (Fig. 11). In spring the PCUC acquired an average width of 25 km, with a nucleus of maximum velocity at 25 km from the shelf, and in summer the current reached a width of 45 km, with a nucleus of maximum velocity at 15 km from the shelf (Fig. 11). The maximum depth of the nucleus at this latitude varied seasonally. In spring and summer it was restricted to 250 m, 260 m in autumn and 280 m in winter, approximately (Fig. 11). Overall, the depth of the maximum poleward current increased with latitude and reached a maximum in winter.

PCUC transport values (Table I) were relatively similar to those computed in the modelling study of Aguirre et al. (2012) and to those reported at 30ºS by Shaffer et al. (1997, 1999). There was relatively significant difference at 35°S from the findings of Leth et al. (2004), who reported a value of 1.3 Sv versus 0.76 Sv in our study. Overall, PCUC transport decreased poleward from a mean value of 0.80 Sv at 30ºS to 0.26 Sv at 39ºS (Table I). The standard deviation of the modelled transport can be as great as 0.4 Sv depending on the latitude and season (see also Fig. 12), due to the model's internal mesoscale variability.

Maximum transport was recorded during spring and summer, with the highest values at 30º and 33°S with 0.94 Sv (spring) and 0.9 Sv (summer), respectively (Fig. 12). At 36°S the transport was lower further north, with the highest values in summer (0.71 Sv) and the lowest in winter (0.22 Sv) (Fig. 12). At 39°S, maximum transport occurred during autumn (0.48 Sv) and minimum transport in winter (0.15 Sv) (Fig. 12). At 39°S during winter/beginning of spring, lower PCUC transport coincided with the lowest values of coast-ocean wind stress (Fig. 9a) and wind stress (Fig. 9c). As wll, wind stress curl between 37° and 40°S was highest between May and October (Fig. 9d), i.e. during the austral winter and spring. The decrease in the intensity of the PCUC towards the pole could be due to lower wind stress and higher wind stress curl towards the south.

3.2. Lagrangian analysis of water masses transported by the PCUC

We investigated the trajectory of the water masses transported by the PCUC, particularly that of water parcels seeded in the PCUC at two zonal sections, at 33°S and at 37°S, to account for alongshore variability.

Approximately ~20% and ~14% of the floats released in the PCUC at 33° and 37°S, respectively, were transported and upwelled in the surface layer in the following six months after leaving the cross-shore sections (Table II). The number of upwelled floats varied little (~1-2%) seasonally in spite of the seasonal variability of the upwelling-favourable winds off Chile. Moreover, the year-to-year variation due to the model’s intrinsic mesoscale variability reached a maximum (~6-7%) in winter (Table II). The majority of the upwelled floats were initially located in the PCUC at depths between 110 m and 130 m (Table II).

Nearly half of the upwelled floats launched at 33°S (50.1% and 47.5% in winter and spring, respectively) were upwelled in a 1° band south of the section, between 33° and 34°S (Fig. 14), while the journey of the floats took ~58.5 and ~38 days, respectively (Fig. 14). High percentages of upwelled floats were found south of the section between 34° and 35°S during autumn (16.1%) and summer (13.8%), taking 132 and 95 days, respectively, to reach the surface (Fig. 14). The number of upwelled floats decreased poleward of 35°S (Fig.14). High percentages of upwelled floats were also recorded north of 33°S, as some water parcels were first transported southward by the PCUC and then transported to the north of the section prior to being upwelled. The recorded values were 23.2% and 22.6% during winter and spring, taking on average 72 and 48 days, respectively, to upwell between 32° and 33°S (Fig. 14). As expected, the lowest percentages were observed several degrees north and south of the section, between 30º and 31°S, with 2.8% of floats emerging after 180 days in winter, and between 37º and 38°S, with 4% of floats emerging after 200 days in summer (Fig. 14).

The majority of the floats launched at 37°S upwelled south of the section. More than half of the floats upwelled between 37° and 38°S in autumn (61.1%) and summer (65.1%), taking 70 and 37 days, respectively (Fig. 15). In contrast to those launched at 33°S, a larger number of the floats (nearly one third in winter and spring) escaped from the PCUC flow, recirculated northward and upwelled between 36° and 37°S. Between 1.4% and 3% of the floats were upwelled further north (33°-34°S).

These results showed that the great majority of the floats (~ 80% at 33°S and ~ 85% at 37°S, Table II) initially transported by the PCUC did not upwell but remained submerged for more than half a year. The situation of subsurface floats differed in winter and summer. In summer they were located respectively +1.5° and +0.3° south of the sections at 33° and 37°S (Table III), while in winter they were located 0° and -0.8° north of the sections at 33°S and 37°S, respectively. Thus, after the floats separated from the PCUC poleward flow, recirculation to the north of their initial positions was more efficient in winter than in summer, and in the south of the region (37°S) than in the north (33°S). The enhanced seasonality at 37°S is consistent with the greater distance from the coast (330 km) of the floats launched in winter than of those launched in summer (263 km). Furthermore, the mean depths of the floats were between 320m (33°S) and 350m (37°S), with very little seasonal changes. The moderate increase (~ 20-30 m) in the mean depth of the floats launched at 33°S and 37°S could be due to the poleward deepening of the PCUC, which allows water at greater depths to be captured by the PCUC flow at 37°S. Overall, these diagnostics suggest that the stirring of water masses transported by the PCUC is more efficient in winter than in summer, and in the south of the domain (37°S) than further north (33°S).

4. Discussion

4.1. Sea level anomaly and eddy kinetic energy (EKE)

Figure 3 shows a comparison of the seasonal SLA averages from simulated and satellite data and reveals substantial discrepancies depending on the season. In autumn, the modelled cyclonic and anticyclonic eddies were more intense than in the AVISO dataset. Some of the modelled anticyclonic structures (e.g. near 33°S;74°W in Fig. 3a) present in both seasons were not observed with altimetry. However, anticyclonic intrathermocline eddies associated with a positive SLA have been observed at this location (Hormazabal et al., 2013).

In spring, during the peak of upwelling-favourable winds (Fig. 9c), the SLA is minimal along the coast for both the model and observations. The strong sea level gradients observed in the model indicated a poleward intensification of the nearshore geostrophic flow. Aguirre et al. (2012) also reported a well-defined jet-like structure during spring and autumn. A Taylor diagram comparing SLA patterns revealed that the model's surface mesoscale activity was 40 to 70% stronger than observed activity, depending on the season. However, the discrepancies may be partly due to data processing. Indeed, the observed SLA maps used in this study were obtained from optimal interpolation of satellite data, processed by AVISO, while the modelled SLA maps resulted from a simple interpolation of the modelled sea level at 1/12° onto the coarser AVISO grid. Further investigation of the impact of the SLA data is beyond the scope of the present study.

The EKEs (Fig. 4) from the simulation and from satellite data differed significantly, with the highest values concentrated in the central zone of the study area (32°-37°S). The simulated EKE pattern was quite similar to that of other climatological simulations by Parada et al. (2012) and Aguirre et al. (2014) for the same region of study. However, the present simulation presented slightly higher maximum values offshore (180 cm^2/s^2) than those from AVISO (160 cm^2/s^2). Closer to the shore between 31° and 36°S the EKE levels were also higher in the model (~80-140 cm^2/s^2) than those calculated from AVISO data (~ 60-80 cm^2/s^2), which could be related to errors in nearshore wind forcing. The intraseasonal waves, which were not introduced in our climatological boundary forcing, may also modify the stability of nearshore flow. Some authors have reported that coastal-trapped waves (CTW), forced by intraseasonal equatorial Kelvin waves (IEKW), have an important impact on coastal hydrography and currents (Hormazabal et al., 2002, 2006). Seasonal CTW, for example, can modify vertical shears between the PCUC and the equatorward surface jet, modulating baroclinic instabilities (Echevin et al., 2011) and thereby the nearshore generation of westward propagating mesoscale eddies (Belmadani et al., 2012). Near the coast of Peru (12°-14°S) and central Chile (26°-30°S) 60-day intraseasonal CTW have a relatively moderate effect (~10%) on EKE (Belmadani et al., 2012), indicating that IEKW-induced CTW enhance EKE near the coast but have a weak impact on the ocean interior (Belmadani et al., 2012). However, further investigation of this issue is beyond the scope of the present study.

4.2. Temperature and salinity

The simulated SST and the Pathfinder data differed, especially nearshore (Fig. 5), where modelled temperature was lower than that in satellite data. The largest biases were found at 35° S (0.9°C) and close to the coast at 38°S (-1.3°C). The cooler than observed near-shore SST is a bias common to ROMS simulations in other EBUS, which is partly explained by a warm bias of ~1-2 °C in the Pathfinder SST (Dufois et al., 2012). This bias can also be partly explained by the over-estimation of the very nearshore wind stress from SCOW data, which cannot resolve the coastal wind drop-off and may thus drive an overly strong coastal upwelling (Renault et al., 2012). Nevertheless, the simulated SST coincided with previous studies (Hormazábal et al., 2001; Letelier et al., 2004) where the annual averages were found to be 12°C at 34°-40°S, and 18°C offshore at 30°-34°S.

The temperature and salinity cross-sections from the simulation compared to CARS data at 32° and 36°S (Fig. 6) also presented some discrepancies. ROMS simulated slightly lower temperature and salinity values than those from in situ observations.

The temperature/salinity diagram (TS) (Fig. 7a) and the water mass percentages in the water column (Fig. 7b) from the simulation compared to the FIP data revealed some differences. In the simulation the low densities observed in the FIP data were not detected, an expected consequence of the exclusion of major rivers in the simulation. As rivers modify the physical and biological properties of the water column via stratification and nutrient and organic matter supply (Iriarte et al., 2012; Sobarzo et al., 2007; Sobarzo and Bravo, 2009; Vargas et al., 2011,), a challenge for future research in the study area (i.e Bío-Bío, Itata, Maipo, Valdivia, etc.) is to incorporate the runoffs from the major rivers into ROMS simulations.

Furthermore, model parameterizations can also induce biases in temperature and salinity. High order diffusive advection schemes in sigma coordinate models such as ROMS may lead to spurious diapycnal mixing. The consequences are that the salinity minimum may erode rapidly along the slope, as for example near the reefs of the steepest islands in the western part of New

Caledonia (Marchesiello et al., 2009). This can lead to the misrepresentation of the low modelled salinity in comparison to *in situ* data from FIP cruises (Fig. 7a).

4.3. Peru-Chile Undercurrent (PCUC)

The velocity range of the main simulated currents was similar to those reported in other modelling studies (Aguirre et al., 2012), especially the PCUC, whose maximum reported transport in this study was 0.94 Sv (Table I) in the northern part of the study area (30°S) during spring, which is close to estimates at the same latitude reported by other authors (1 Sv; Pizarro et al. 2002; Shaffer et al., 1997, 1999). Leth et al. (2004) estimated the geostrophic transport of the PCUC from Profiling CTD (Conductivity, Temperature and Depth) data collected at different latitudes taken in May–June 1995 along 28°- 35°S off the Chilean coast to 86°-88°W. They estimated geostrophic transport of the PCUC of 1.3 Sv at 28°S and 35°S, and 1.1 Sv at 43°S. These values are higher than those in our simulation, which could be attributed to the fact that the *in situ* measurements in Leth et al. (2004) are “snapshots” of PCUC transport, while our measurements are climatological means. Furthermore, the model does not realistically represent the spreading of isotherms at 36°S (Fig. 6c), which could partly explain the discrepancy.

The modelled PCUC displayed latitudinal changes, with velocity (Figs. 8 and 10a) and transport decreasing poleward (Fig. 12). Such latitudinal variation was reported by Silva and Neshyba (1979), who estimated an average poleward velocity in the core of 5-10 cm/s from 20° to 30°S, decreasing to 0-5 cm/s from Valparaiso (33°S) southward. Fonseca (1989) reported that this undercurrent maintained a seasonal cycle, with the highest level of transport (off the shelf) occurring during summer. Its core is located around 150 to 200 m, with a characteristic maximum geostrophic velocity of about 20 cm/s.

In order to investigate the link between current and wind forcing, we compared PCUC transport to Sverdrup transport (Sverdrup, 1947), which relates vertically integrated meridional mass transport in the interior ocean to open ocean wind stress curl. Sverdrup transport was computed over two coastal bands 50 and 100 km wide using the SCOW wind stress curl (Figs. 2 and 9). Mean Sverdrup transport computed in the 50 km band (Table IV) was in reasonable agreement with the modeled transport at 30° and 36°S, but not at 33°S and 39°S. In the 100 km band (Table IV) there was a relative agreement at 30°S and a 50% discrepancy at 36°S. The standard deviation of the modelled transport associated with internal interannual variability is greater than the mean, except at 39°S. Aguirre et al. (2012) also compared the modelled transport between 90°W and the coast to Sverdrup transport computed from Quikscat data and found a reasonable agreement (within ~ 20-30% of error) away from the coast (between 90° and 80°W) and strong discrepancies nearshore. The Sverdrup transport they obtained in the 100-200 km coastal band was much lower (*i.e.* ~0.3 Sv at 30°S) than in our case (~1.4-1.5 Sv, Table IV). Sverdrup transport may be underestimated nearshore when using low-resolution wind products that do not represent the strong drop-off close to the coast (e.g. Renault et al., 2015). Thus the weaker nearshore wind stress curl near the coast, associated with the coarser (0.5°) Quikscat wind product that they used may explain the discrepancies between our results and those of Aguirre et al. (2012). These results suggest that the PCUC mean flow is partly explained by simple wind-forced Sverdrup theory at some locations along the Chile coast, but not in all the studied area.

Aguirre et al. (2012) further investigated the role of wind stress curl on the dynamics of the near-surface alongshore flow off central Chile with a no-curl wind forcing ROMS model. They found little impact of the curl on the vertical PCUC structure at 30° and 36°S, and a decrease in PCUC intensity at 36°S.

The dynamic impact of the curl on the undercurrent may also occur in other EBUS where strong coastal wind stress curl is observed. Pedlosky (1974) indicates that a poleward undercurrent along an eastern boundary benefits from negative (in the Southern Hemisphere) wind stress curl along the coast. Marchesiello et al. (2003) reported that the regional model (ROMS) and Sverdrup transports were consistent in the California current system., Albert et al. (2010) showed that strong upwelling-favorable nearshore wind stress curl in the Peru upwelling system induces shoaling of the coastal undercurrent and a wide productive coastal zone through upwelling of nutrient−replete waters.

The PCUC is of crucial importance because it carries equatorial subsurface water along the coasts of Peru (Montes et al., 2010) and Chile and disperses it offshore through coherent anticyclones with salty cores (Colas et al., 2012). Intrathermocline eddies, which break off from the PCUC near 37°S, move northeast at a speed of ~2 km day^{-1}, which represents an average westward flux of ~1 Sv (Hormazábal et al., 2013). This mass flux is on the same order of magnitude as the PCUC flux reported by Shaffer et al. (1997, 1999) and in this study (Table I). Furthermore, the PCUC flux decreases significantly between 36° and 39°S, suggesting that a large portion of PCUC water is trapped in intrathermocline eddies and dispersed offshore (Fig. 10b).

Other aspects of the simulation are the changes in PCUC width and nucleus depth. The PCUC generally presented a mean latitudinal climatological width of 60 km, with lower values (15 km in spring) around 39°S (Fig. 11). The nucleus of maximum current velocity was located at a depth of approximately 120m at 30°S, and deepened further south in the study area, reaching ~218m at 33°S, ~230m at 36°S, and ~260m at 39°S (Fig. 13). The nucleus deepened in winter at all studied latitudes, and became shallower during spring-summer. In previously reported observations, the PCUC nucleus was found at depths of 180 m (2 years record, Shaffer et al., 1995) and 220 m (6-year record, Shaffer et al., 1999) at 30°S, with a maximum velocity of 12.8 cm/s. This result differs slightly from ours as we obtained an average velocity core of 10 cm/s at 120m depth at 30° S (Fig. 13). Leth et al. (2004) found alongshore differences in poleward velocity, revealing maxima of 7.6 cm/s at 163m (28°S), 11.8 cm/s at 190m (35°S) and 9.5 cm/s at 253m (43°S) (Fig 13). Silva and Neshyba (1979) also found evidence of a high velocity nucleus that deepens towards the poles in the PCUC.

The deepening also occurs in other EBUS. Mittelstaedt (1976) and Barton (1989) reported the nucleus of the poleward undercurrent off the northeast coast of Africa, which deepens as it extends polewards (Barton, 1989; Clarke, 1989; Mittelstaedt, 1991). Off the US west coast, Pierce et al. (2000) observed a deepening undercurrrent, consistent with PV conservation.

Using ROMS in the Peru region, Penven et al. (2005) found a clear deepening of the PCUC's lower limit, which was trapped along the slope. In our case, while the upper part of the PCUC sometimes outcropped as a counter current (e.g. between 33° and 39°S, Fig. 8b-d), the depth of the bottom of this poleward undercurrent varied meridionally so that planetary vorticity f/H was conserved over a range of latitudes (where f is the Coriolis parameter and H the thickness of the PCUC layer). Our present results do not seem to be consistent with those reported by Penven et al. (2005) since the thickness of the bottom-trapped PCUC is clearly thinner south of 33°S (Fig. 8). However, the bias in isopycnal spreading at 36°S (Fig.6c) also suggests there is a bias in PCUC thickness in this latitude range, so the f/H theory cannot be ruled out.

Other authors have tried to explain the deepening of the PCUC. For example, Pizarro (1999) used the approach of McCreary (1981), which showed that a linear model driven by alongshore wind could represent the deepening of the California undercurrent poleward of the wind patch, without invoking the role of wind-stress curl. Pizarro (1999) applied this model to the PCUC and found a clear poleward deepening of the PCUC core (marked by the 0.1 m s^{-1} isoline in his study) between 30° and 35°S from ~450 m to ~600 m. PCUC velocities in this case were roughly twice as high as those generated in our simulation. In our case, the depth of the simulated PCUC lower limit (e.g. marked by the 0.05 m s^{-1} isoline) only slightly decreased from 30° to 33°S (Fig. 8a-b). Their model also showed slight poleward intensification and widening of the PCUC core, which were not identified in our case. This simplified model did not take into account the effects of the seafloor topography, the curved coastline or nonlinear rectification of the current.

4.4. Upwelling and PCUC water mass pathways

To determine the paths of particles transported by the PCUC and the time necessary for them to upwell to the surface (up to 50 m), virtual floats were released into the current at 33° and 37°S. The average duration of the journeys of floats that upwelled was determined for each season. Most upwelled floats from both latitudes travelled southward along the PCUC and were upwelled south of the release sections. The highest percentages of upwelled floats were recorded at latitudes close to the area of release. For example, 40% of floats released at 33°S upwelled between 33° and 34°S and took on average 50 days to reach a depth of 50 m (Fig. 14). Similarly, over 50% of floats released at 37°S upwelled between 37° and 38° S and took approximately 56 days to do so (Fig. 15). However, a significant percentage of floats changed direction and ended up north of the sections. They were likely transported north via surface currents (at depths greater than 50 m) induced by wind forcing or trapped and transported by currents associated with subsurface eddies. Some authors have described the presence of intrathermocline eddies (Hormazabal et al. 2013; Leth and Middleton, 2004) generated by baroclinic instabilities around 37°S (Punta Lavapie). These eddies, which transport nutrients and low oxygen concentrations offshore, may also transport particles north (Figs. 14 and 15), making it quite complex to determine the origin of particles reaching the surface during upwelling.

Moreover, the percentage of particles that effectively reached the surface via upwelling did not exceed 20% at either 33°S or 37°S. Small seasonal differences were detected at 33°S, with 19.2% and 20.2% of particles emerging in spring and winter, respectively (Table II). These small seasonal differences may be associated with wind stress values used to force the simulation, which were climatological and did not represent daily and synoptic frequencies, and which have been described as the main components of the wind stress along the coastal of central-southern Chile (Sobarzo et al., 2007, 2010). Results in line with the present study were found in a numerical study of upwelling source waters in the California upwelling off Oregon (Rivas and Samelson, 2010). Using Lagrangian diagnostics to identify the origin and depth of upwelled waters, they found that the modelled poleward undercurrent, with a similar depth range as in our case, only made a small direct contribution to the source waters in a climatological simulation comparable to ours, and that this proportion decreased with high frequency wind forcing of nearshore dynamics. Thus, the impact of high frequency winds on the trajectory of PCUC water masses should be considered in future work.

5. Conclusions

The simulation results are consistent with observed spatial patterns in most of the analysed variables. For example, EKE showed high values in a narrow band along the coast (from 30° to 37°S), and a decline south of this zone, but simulated EKEs were higher, particularly between 30° and 38°S in a coastal strip of 200-300 km.

The simulated average field of SST exhibited low SST values near the coast due to the upwelling of cool waters, but these were slightly lower than those of the Pathfinder data, which is likely due to the overestimation of the nearshore wind stress from SCOW data used in this ROMS simulation. The monthly climatological wind used here does not represent the alternation of highly frequent upwelling and relaxing events, which may also affect the model SST. Annual averages of simulated temperature at 32° and 36°S compared well to real data. In these latitudes, the model and observed isotherm shoaling to the shore both indicated active upwelling. Nevertheless, the model failed to accurately represent thermal stratification in the first 100 m (of 50-300 km) observed in CARS data. The yearly averages of simulated salinity cross-sections at 32° and 36°S also compared well to CARS data. It was observed in the model that maximum subsurface salinity was located near the coast at a depth of approximately 250 m, associated with the PCUC.

The density values from the model and from cruises during summer months (at 35.5º-40°S; 72.75º-77.8°W) were very similar. However, low water densities were not appropriately represented in the simulation (Fig. 7). This could be an effect of the exclusion of major rivers in the simulation. Additionally diffusive advection schemes in sigma coordinate models may lead to spurious diapycnal mixing and errors in salinity.

The velocity and transport of the simulated PCUC decreased poleward, which agrees well with the results previously reported for this area (Leth and Shaffer 2001; Pizarro et al. 2002; Shaffer et al. 2004). In some latitudes a link was observed between the PCUC and the surface poleward PCCC flow, which was intense in summer and spring. The average width of the PCUC also changed toward the south of the study area, with approximately 50 km at 30° and 33°S, ~100 km at 36°S and ~ 30 km at 39°S. The abrupt width changes at 36°S may be the result of changes in topography, the presence of an irregular coastline or intrathermocline eddies that alter the undercurrent at this latitude range. In addition, our results showed that the core of maximum velocity of PCUC deepened from ~120 m at 30°S to ~250 m at 39°S, which is in agreement with what has been reported for other poleward undercurrents (e.g. California; Thomson and Krassovski, 2010).

Twenty and 14% of the Lagrangian floats transported from 33º and 37ºS respectively, were observed in the surface layer (50 m) 6 months after release. At these latitudes, most of the upwelled floats travelled southward along the PCUC and were upwelled south of the launch sections. The highest percentages of upwelled floats were found at latitudes adjacent to the release zones. A large portion of them altered their trajectory and ended up north of the sections, probably conducted north by surface currents driven by wind forcing or by subsurface eddies.

The large majority of the floats transported by the PCUC did not upwell but remained submerged for more than 6 months. In both latitude ranges (33º and 37ºS), more floats recirculated to the north of the sections in winter than in summer. This suggests that the mixing of PCUC water with offshore waters was more intense during winter and spring than during summer and fall.

The simulations in this study improve our understanding of alongshore circulation and seasonal variability of nearshore circulation in the HCS. Studying the dynamics of the PCUC and the characteristics (origin, trajectory) of the transported water mass is a first step towards a more comprehensive study of the coupled physical-biogeochemical processes that drive the thriving productivity of the HCS. This will be the purpose of future work.

Acknowledgements

This study was funded by the Interdisciplinary Center for Aquaculture Research (INCAR; FONDAP Project N°15110027; CONICYT). Odette Vergara was also supported by a Doctoral Scholarship from the Comisión Nacional de Investigación Científica y Tecnológica (CONICYT, Ministry of Education, Chile). We acknowledge the financial support for O. Vergara's internships at LOCEAN received from the French Embassy in Chile, the REDOC. CTA (Red Doctoral en Ciencia, Tecnología y Ambiente, University of Concepción, Chile) and LIA MORFUN (International Associated Laboratory) project (LIA 1035 CNRS).

6. References

Aguirre, C., Pizarro, O., Strub, P.T., Garreaud, R., Barth, J., 2012. Seasonal dynamics of the near-surface alongshore flow off central Chile. J. Geophys. Res. 117, 1-17.

Aguirre, C., Garreaud, R., Rutllant, J.A., 2014. Surface ocean response to synoptic-scale variability in wind stress and heat fluxes off south-central Chile. Dyn. Atmos. Ocean. 65, 64-85.

Aiken, C. M., Navarrete, S. A., Pelegri, J. L., 2011. Potential changes in larval dispersal and alongshore connectivity on the central Chilean coast due to an altered wind climate. J. Geophys. Res. 116, 1-14.

Albert, A., Echevin, V., Lévy, M., Aumont, O., 2010. Impact of nearshore wind stress curl on coastal circulation and primary productivity in the Peru upwelling system. J. Geophys. Res. 115, 1-13.

Bakun A., 1990. Global climate change and intensification of coastal upwelling. Science. 247, 198-201.

Bakun, A., Field, D. B., Redondo-Rodríguez, A., Weeks, S. J., 2010. Greenhouse gas, upwelling favorable winds, and the future of coastal ocean upwelling ecosystems. Glob. Chan. Biol. 16, 1213-1228.

Barnier, B., Siefridt, L., Marchesiello, P., 1995. Thermal forcing for a global ocean circulation model using a three-year climatology of ECMWF analyses. J. Mar. Syst. 6, 363–380.

Barton, E.D., 1989. The poleward undercurrent on the eastern boundary of the subtropical North Atlantic. Coast. Estuar. Stud. 34, 82–95.

Barton, E.D., 1998. Eastern boundary of the North Atlantic-northwest Africa and Iberia, in: Robinson, A., R., Brink, K., H. (Eds.), The Sea, Vol. 11. Global Coastal Ocean: regional Studies and Synthesis. John Wiley and Sons, New York, pp. 633-657.

Batteen, M. L., Hu, C-P., Bacon, J. L. Nelson, C.S., 1995. A Numerical Study of the Effects of Wind Forcing on the Chile Current System. J. Oceanog. 51, 585-614.

Becker JJ, Sandwell DT, Smith W et al (2009) Global Bathymetry and elevation data at 30 arc seconds resolution: SRTM30 PLUS. Marine Geodesy 32:355–371

Belmadani, A., Echevin, V., Dewitte, B., Colas, F., 2012. Equatorially forced intraseasonal propagations along the Peru-Chile coast and their relation with the nearshore eddy activity in 1992–2000: A modeling study, J. Geophys. Res. 117, 1-20.

Belmadani, A., Echevín, V., Codron, F., Takahashi, K., Junquas, C., 2014. What dynamics drive future winds scenarios for coastal upwelling off Peru and Chile? Clim. Dyn. 43 (7-8), 1893-1914.

Bernal, P., Robles, L., Rojas, O., 1982. Variabilidad física y biológica en la región meridional del sistema de corrientes Chile-Perú. Mon. Biol., Pontificia Universidad Católica de Chile. 2, 75-102.

Blanke, B., Arhan, M., Lazar, A., Prévost, G., 2002. A Lagrangian numerical investigation of the origins and fates of the salinity maximum water in the Atlantic. J. Geophs. Res. 107 (C10), 1-15.

Blumberg, A. F., Mellor, G. L., 1987. A description of a three- dimensional coastal ocean circulation model, in Three-Dimensional Coastal Ocean Models, in: N. Heaps (Eds.), Coastal Estuarine Series 4, AGU, Washington, D. C. pp. 1–16

Brochier, T., Echevin, V., Tam, J., Chaigneau, A., Goubanova, K., Bertrand, A., 2013. Climate change scenarios experiments predict a future reduction in small pelagic fish recruitment in the Humboldt Current system. Glob. Chan. Biol. 19, 1841-1853.

Capet, X. J., Marchesiello, P., McWilliamns, J. C., 2004. Upwelling response to coastal wind profiles. Geophys. Res. Lett. 31, 1-4.

Capet, A., E. Mason, V. Rossi, C. Troupin, Y. Faugère, I. Pujol, and A. Pascual (2014), Implications of refined altimetry on estimates of mesoscale activity and eddy-driven offshore transport in the Eastern Boundary Upwelling Systems, Geophys. Res. Lett. , 41 , 7602–7610, doi:10.1002/2014GL061770

Carr, S., Capet, X., McWilliams, J. C., Pennington, J. T., Chávez, F.P., 2008. The influence of diel vertical migration on zooplancton transport and recruitment in an upwelling region: Estiamtes from a coupled behaviorial-physical model. Fish. Oceanog. 17, 1-15.

Casey, K.S., Brandon, T.B., Cornillon, P., Evans, R., 2010. The past, present and future of the AVHRR Pathfinder SST program, in: Gower, J.F.R., Barale, V., Alberotanza, L. (Eds.), Oceanography from Space. Revisited. Springer.

Chaigneau, A., Dominguez, N., Eldin, G., Vasquez, L., Flores, R., Grados, C., Echevin. V., 2013. Near-coastal circulation in the Northern Humboldt Current System from shipboard ADCP data. J. Geophys. Res. Oceans. 118, 1-16.

Chávez, F.P., Ryan, J., Lluch-Cota, S.E., Niquen, M., 2003. From anchovies to sardines and back: multidecadal change in the Pacific Ocean. Science. 299, 217–221.

Chávez, F. P., Bertrand, A., Guevara-Carrasco, R., Soler, P., Csirke, J., 2008. The northern Humboldt Current System: Brief history, present status and a view towards the future. Prog. Oceanogr. 79, 95–105.

Clarke, A. J. 1989. Theoretical understanding of eastern ocean boundary poleward currents, , in: Neshyba, S. J., Mooers, Ch. N. K., Smith, R. L., Barber, R. T. (Eds.), Poleward Flows Along Eastern Ocean Boundaries. Springer-Verlag, New York Inc., pp. 26–39.

Codispoti, L.A., Barber, R.T., Friederich, G. E., 1989. Do nitrogen transformations in the poleward undercurrent off Perú and Chile have a globally significant influence? in: Neshyba, S. J., Mooers, Ch. N. K., Smith, R. L., Barber, R. T. (Eds.), Poleward Flows along Eastern Ocean Boundaries. Springer-Verlag, New York Inc., pp. 281-314.

Colas, F., Capet, X., McWilliams, J. C., Shchepetkin, A., 2008. 1997–98 El Niño off Peru: A numerical study. Prog. Oceanogr. 79, 138–155.

Colas, F., McWilliams, J. C., Capet, X., Kurian, J., 2012. Heat balance and eddies in the Peru-Chile current system, Clim. Dyn. 39 (1-2), 509-529.

Cubillos, L. A., Arancibia, H., 1993. On the seasonal growth of common sardine (Strangomera bentincki) and anchovy (Engraulis ringens) off Talcahuano, Chile. Rev. Biol. Mar. 28, 43-49.

Cubillos, L. A., Bucarey, D., Canales, M., 2002. Monthly abundant estimation for common sardine Strangomera bentincki and anchovy Engraulis ringens in the central-southern area off Chile (34º-40°S). Fish. Res. 57, 117-130.

Cubillos, L. A., Ruiz, P., Claramunt, G., Gacitúa, S., Núñez, S., Castro, L. R., Riquelme, K., Alarcón, C., Oyarzún, C., Sepúlveda, A., 2007. Spawning, daily egg production, and spawning stock biomass estimation for common sardine (*Strangomera bentincki*) and anchovy (*Engraulis ringens*) off central southern Chile in 2002. Fish. Res. 86, 228-240.

Czeschel, R., Stramma, L., Schwarzkopf, F. U., Giese, B., S., Funk, A., Karstensen, J., 2011. Mid depth circulation of the eastern tropical South Pacific and its link to the oxygen minimum zone. J. Geophys. Res. 116 (C01015), 1-13.

Daneri, G., Dellarossa, V., Quiñones, R., Jacob, B., Montero. P., Ulloa, O., 2000. Primary production and community respiration in the Humboldt Current System off Chile and associated oceanic areas. Mar. Ecol. Prog. Ser. 197, 41-49.

da Silva, A. M., Young, C. C., Levitus, S. (Eds.)., 1994. Atlas of Surface Marine Data 1994, vol. 1. Algorithms and Procedures. NOAA Atlas NESDIS, vol. 6. Technical Report. U. S., NOAA, Silver, Spring, MD. 83 pp.

Dufois, F., Penven, P., Whittle, C., Veitch, J., 2012. On the warm nearshore bias in Pathfinder monthly SST products over Eastern Boundary Upwelling Systems. Ocean Modell. 47, 113-118.

Dunn, J.R., Ridgway, K.R., 2002. Mapping ocean properties in regions of complex topography. Deep Sea Res. 49 (3), 591–604.

Echevin, V., Colas, F., Chaigneau, A., Penven, P., 2011. Sensitivity of the Northern Humboldt Current System nearshore modeled circulation to initial and boundary conditions. J. Geophys. Res., 116 (C07002), 1-16.

Echevin, V., Albert, A., Lévy, A., Graco, M., Aumont, O., Piétri, A.,Garric, G., 2014. Intraseasonal variability of nearshore productivity in the Northern Humboldt Current System: The role of coastal trapped waves. Cont. Shelf Res. 73, 14-30.

Fonseca, T., 1989. An overview of the poleward undercurrent and upwelling along the Chilean coast, in: Poleward Flows Along Eastern Ocean Boundaries, Neshyba, S. J., Mooers, Ch. N. K., Smith, R. L., Barber, R. T. (Eds.), Springer-Verlag, New York Inc. pp. 203-228.

Freitag, H. P., Halpern, D., 1981. Hydrographic observations off Northern California during May 1977. J. Geophys. Res. 86, 4248–4252.

Fuenzalida, R., Schneider, W., Garcés-Vargas, J., Bravo, L., 2008. Satellite altimetry data reveal jet-like dynamics of the Humboldt Current. J. Geophys. Res. 113, 1-11.

Fuenzalida, R., Schneider, W., Garcés-Vargas, J., Bravo, L., Lange, C., 2009. Vertical and horizontal extension of the oxygen minimum zone in the eastern South Pacific Ocean. Deep Sea Res. II. 56(16), 992-1003.

Garreaud, R., Falvey, M., 2009. The coastal winds off western subtropical South America in future climate scenarios. Int. J. Climatol. 29, 543-554.

Gay, P. S., Chereskin, T. K., 2009. Mean structure and seasonal variability of the poleward undercurrent off southern California. J. Geophs. Res. Oceans. 114, 1-17.

Gruber, N., Hauri, C., Lachkar, Z., Loher, D., Froelicher, T. L., Plattner, G.-K., 2012. Rapid progression of ocean acidification in the California Current System. Science. 337, 220–223.

Gunther, E.R., 1936. Variations in behaviour of the Perú Coastal Current: with an historical introduction. The Geograph. J. 88, 37–61.

Gutiérrez, D., Bouloubassi, I., Sifeddine, A., Purca, S., Goubanova, K., Graco, M., Field, D., Méjanelle, L., Velazco, F., Lorre, A., Salvatteci, R., Quispe, D., Vargas, G., Dewitte, B., Ortlieb, L., 2011. Coastal cooling and increased productivity in the main upwelling zone off Peru since the mid- twentieth century, Geophys. Res. Lett. 38, 1-6.

Haynes, R., Barton, E. D., 1990. A poleward flow along the Atlantic coast of the Iberian Peninsula. J. Geophys. Res. 95, 11425-11442.

Hernández-Miranda, E., Quiñones, R. A., Aedo, G., Valenzuela, A., Mermoud, N., Román, C., Yañez, F., 2010. A major fish stranding caused by a natural hypoxic event in a shallow bay of the eastern South Pacific. J. Fish Biol. 76, 1543-1564.

Hickey, B, M., 1979. The California Current System-hypotheses and facts. Prog. Oceanog. 4(8), 191-279.

Hill, A. E., Hickey, B. M., Shillington, F. A., Strub, P. T., Brink, K. H., Barton, E. D., Thomas, A.

C., 1998. Eastern ocean boundaries coastal segment (e), in: Robinson, A. R. Brink, H. K., (Eds.), The Sea, vol. 11, The Global Coastal Ocean: Regio- nal Studies and Syntheses. John Wiley, New York, pp. 29–67.

Hormazábal, S., Shaffer, G., Letelier, J., Ulloa, O., 2001. Local and remote forcing of sea surface temperature in the coastal upwelling system off Chile. J. Geophys. Res. 106, 16.657-16.671.

Hormazábal, S., Shaffer, G., Silva, N., Navarro, E., 2006. The Peru Chile undercurrent and the oxygen minimum zone variability off central Chile. Gayana. 70(1), 37–45.

Hormazábal, S., Combes, V., Morales, C.E., Correa-Ramírez, M. A., Di Lorenzo, E., Nuñez, S., 2013. Intrathermocline eddies in the coastal transition zone off central Chile (31-41°S). J. Geophys. Res. Oceans. 118, 1-11.

Huyer, A., Smith, R. L., Paluszkiewicz, T., 1987. Coastal upwelling off Peru during normal and El Niño times, 1981-1984. J. Geophys. Res. 92(C13), 14297-14307.

Iriarte, J. L., Vargas, C., Tapia, F. J., Bermúdez, R., Urrutia, R.E., 2012. Primary production and plankton carbon biomass in a river-influenced upwelling area off Concepción, Chile. Prog. Oceanogr. 92 (1), 97-109.

Large, W. G., McWilliams, J. C.,. Doney, S. C., 1994. Oceanic vertical mixing: a review and a model with a nonlocal boundary layer parameterization. Rev. Geophys. 32, 363-403.

Letelier, J., Pizarro, O., Núñez, S., Arcos, D., 2004. Spatial and temporal variability of thermal fronts off central Chile (33–40°S). Gayana. 38, 358–362.

Leth, O., Middleton, J. F., 2004. A mechanism for enhanced upwelling off central Chile: Eddy advection. J. Geophys. Res. 109, 1-17.

Leth, O., Shaffer, G., 2001. A numerical study of the seasonal var- iability in the circulation off central Chile, J. Geophys. Res.106, 229-248.

Leth, O., Shaffer, G., Ulloa, O., 2004. Hydrography of the eastern South Pacific Ocean: Results from the Sonne 102 cruise, May–June 1995, Deep Sea Res. II. 51, 2349–2369.

Marchesiello, P., McWilliams, J.C., Shchepetkin, A., 2001. Open boundary conditions for long-term integration of regional oceanic models. Ocean Model. 3 (1–2), 1–20.

Marchesiello P., McWilliams, J.C., Shchepetkin, A., 2003. Equilibrium structure and dynamics of the California Current System. J. Phys. Oceanogr. 33, 753-783.

Marchesiello P., Debreu, L., Couvelard, X., 2009. Spurious diapycnal mixing in terrain-following coordinate models: the problem and a solution. Ocean Model. 26, 156-169.

Marchesiello P., Estrade, P., 2009. Eddy activity and mixing in upwelling systems: a comparative study of Northwest Africa and California regions. Int. J. Earth Sci. 98 (2), 299-308.

Mason, E., Colas, F., Pelegrí, J. L., A Lagrangian study tracing water parcels origins in the Canary Upwelling System. Sci. Mar. 76S1, 79-94.

Mason, E., Molemaker, J., Shchepetkin, A. F., Colas, F., McWilliams, J. C., Sangrà, P., 2010. Procedures for offline grid nesting in regional ocean models. Ocean Model. 35, 1–15.

Mesias, J., R.Matano, and P. T. Strub. 2001. Anumerical study of the upwelling circulation off central Chile, J. Geophys. Res. 106, 611–623.

Mittelstaedt, E., 1976. On the currents along the Northwest African coast south of 221 North. Dtsch. Hydrog. Z. 29, 97–117.

Mittelstaedt, M. 1991. The ocean boundary along the northwest African coast: Circulation and oceanographic properties at the sea surface. Prog. Oceanogr. 26, 307-355.

McCreary, J. P., 1981. A linear stratified ocean model of the coastal undercurrent. Phil Trans. R. Soc. Lond. A: 1981302 3885-413; doi: 10.1098/rsta. 1981.0176.

McCreary, J.P., Chao, S.-Y., 1985. Three-dimensional shelf circulation along an eastern ocean boundary. J. Mar. Res. 43 (1), 13–36.

Montero, P., Daneri, G., Cuevas, L.A., González, H.E., Jacob, B., Lizárraga, L., Menschel, E., 2007. Productivity cycles in the coastal upwelling area off Concepción: the importance of diatoms and bacterioplankton in the organic carbon flux. Prog. Oceanogr. 75, 518–530.

Montes, I., Colas, F., Capet, X., Schneider, W., 2010. On the pathways of the equatorial subsurface currents in the eastern equatorial Pacific and their contributions to the Peru-Chile Undercurrent. J. Geophys. Res. 115, 1-16.

Neshyba, S. J., Mooers, C. N. K., Smith, R. L., Barber, R. T. (Eds.), 1989, in: Poleward Flows Along Eastern Ocean Boundaries, Coastal and Estuarine Studies, vol. 34. Springer-Verlag New York, Inc., pp. 374

Oerder, V., Colas, F., Echevin, V., Codron, F., Tam, J.,. Belmadani, A., 2015. Peru-Chile upwelling dynamics under climate change. J. Geophys. Res. 120, 1152-1172.

Parada, C., Colas, F., Soto-Mendoza, S., Castro, L., 2012. Effects of seasonal variability in across- and alongshore transport of anchoveta (*Engraulis ringens*) larvae on model-based pre-recruitment indices off central Chile. Progr. Oceanogr. 92 (1), 192-205.

Pauly, D., Christensen, V., 1995. Primary production required to sustain global fisher- ies. Nature. 374, 255–257.

Pedlosky, J., 1974. Longshore currents, upwelling and bottom topography. J. Phys. Oceanogr. 4, 214–226

Penven, P., Debreu, L., Marchesiello, P., McWilliams, J. C., 2006. Evaluation and application of the ROMS 1-way embedding procedure to the central California upwelling system. Ocean Model. 12, 157-187.

Penven, P., Echevin,V., Pasapera, J., Colas, F., Tam, J., 2005. Average circulation, seasonal cycle and mesoscale dynamics of the Perú Current System: A modeling approach, J. Geophys. Res. 110, 1-21.

Pierce, S.D., Smith, R.L., Kosro, P.M., Barth, J.A., Wilson, C.D., 2000. Continuity of the poleward undercurrent along the eastern boundary of the mid-latitude Pacific. Deep-Sea Res. 47, 811–829

Pizarro, O. 1999. Low frequency fluctuations in the Eastern Boundary Current off South America: Remote and local forcing. Ph. D. Thesis. Earth Sciences Centre, Göteborg, Sweeden. 102 pp.

Pizarro, O., Shaffer, G., Dewitte, B., Ramos, M., 2002. Dynamics of seasonal and interanual variability of the Peru–Chile undercurrent. Geophys. Res. Lett. 29 (12), 1-4.

Quiñones, R. A., Gutiérrez, M.H., Daneri, G., Gutiérrez, D., González, H.E., Chávez, F., 2010. The Humboldt Current System, in: Liu, K. K., Atkinson, L., Quiñones, R. A., Talaue-McManus, L. (Eds.), Carbon and nutrient fluxes in global continental margins, IGBP Series Book, Springer-Verlag, New York, pp. 44-64.

Ramos, M., Pizarro, O., Bravo, L., Dewitte, B., 2006. Seasonal variability of the permanent thermocline off northern Chile. Geophy. Res. Lett. 33, 1-6.

Renault, L., Dewitte, B., Marchesiello, P., Illig, S., Echevin, V., Cambon, G., Ramos, M., Astudillo, O., Minnis, P., Ayers, J. K., 2012. Upwelling response to atmospheric coastal jets off central Chile: A modeling study of the October 2000 event, J. Geophys. Res. 117 (C02030), 1-21.

Ridway, K.R., Dunn, J.R., Wilkin, J.L., 2002. Ocean interpolation by four-dimensional least squares—applications to the waters around Australia. J. Atmos. Ocean Technol. 19 (9), 1357–1375.

Risien, C.M., Chelton, D.B., 2008. A global climatology of surface wind stress field from eight years of QuiKSCAT Scatterometer Data. J. Phys. Oceanogr. 38, 2379-2413.

Rivas, D., and R.M. Samelson, 2010. A numerical modeling study of the upwelling source waters along the Oregon coast during 2005. J. Phys. Oceanogr., 41, 88-112, DOI: 10.1175/2010JPO4327.1

Shaffer, G., Hormazábal, S., Pizarro, O., Djurfeldt, L., Salinas, S., 1999. Seasonal and interannual variability of currents and temperature over the slope off central Chile. J. Geophys. Res. 104, 951–961.

Shaffer, G., Hormazábal, S., Pizarro, O., Ramos, M., 2004. Circulation and variability in the Chile Basin. Deep Sea Res. I. 51, 1367– 1386.

Shaffer, G., Pizarro, O., Djurfeldt, L., Salinas, S., Rutllant, J., 1997. Circulation and low-frequency variability near the Chile coast: remotely forced fluctuations during the 1991–1992 El Niño. J. Phys. Oceanogr. 27, 217–235.

Shaffer, G., Salinas, S., Pizarro, O., Vega, A., Hormazábal, S., 1995. Currents in the deep-ocean off Chile (30°S). Deep-Sea Res. I. 42, 425–436.

Schneider, W., Fuenzalida, R., Garcés, J., 2004. Corrientes marinas y masas de agua, in: Werlinger, C. (Ed.), Biología Marina y Oceanografía: Conceptos y Procesos, Vol. I. Trama Impresores S.A., Chile, pp. 177-194.

Shchepetkin, A., McWilliams, J. C., 2005. The regional oceanic modeling system (ROMS): A split-explicit, free-surface, topography-following- coordinate oceanic model. Ocean Model. 9, 347–404.

Silva, S., Fonseca, T., 1983. Geostrophic component of the northem flow off northern Chile, in: Arana, P. (Ed.), Conferencia Internacional Sobre Recursos Marinos del Pacifico, pp. 59-70.

Silva, N., Konow, D., 1975. Contribución al conocimiento de las masas de agua en el Pacífico Sudoriental. Expedición Krill. Crucero 3-4. Julio-agosto 1974. Rev. Com. Perm. Pacífico Sur. 3, 63-75.

Silva, N., Neshyba, S., 1979. On the southernmost extension of the Perú-Chile Undercurrent. Deep Sea Res. 26, 1387–1393.

Silva, N., Rojas, N., Fedele, A., 2009. Water masses in the Humboldt Current System: Properties, distribution, and the nitrate deficit as a chemical water mass tracer for equatorial subsurface water off Chile. Deep-Sea Res. II. 56, 1004–1020.

Sobarzo, M., Bravo, L., 2009. Dinámica de las corrientes asociadas a la plataforma continental interior frente a la desembocadura del río Itata, in: Parra, O., Castilla, J. C., Romero, H., Quiñones, R. A., Camaño, A. (Eds.), La cuenca hidrográfica del Itata: Aportes científicos para su gestión sustentable. Ediciones Universidad de Concepción, Concepción, Chile, pp. 175-161.

Sobarzo, M., Bravo, L., Donoso, D., Garcés-Vargas, J., Schneider, W., 2007. Coastal upwelling and seasonal cycles that influences the water column over the continental shelf of central Chile. Progr. Oceanogr. 75, 363-382.

Soto-Mendoza, S., Parada, C., Castro, L., Colas, F., Schneider, W., 2012. Modeling transport and survival of anchoveta eggs and yolk-sac larvae in the coastal zone off central-south Chile: Assessing spatial and temporal spawning parameters. Progr. Oceanogr. 92(1), 178-191.

Strub, P. T., Mesías, J., Montecino, V., Ruttlant, J., Salinas, S., 1998. Coastal ocean circulation off western South America. Coastal Segment (6,E), in: Robinson, A., Brink, K. (Eds), The Sea, Vol. 11. John Wiley & Sons, Hoboken, pp. 273-313

Strub, P. T., Mesias, M., James, C., 1995. Altimeter observations of the Perú-Chile Countercurrent. Geophys. Res. Lett. 22, 211–214.

Sverdrup, H. U. 1947. Wind-driven currents in a baroclinic ocean with application to the equatorial currents of the eastern Pacific. Proc. Natl. Acad. Sci. U.S.A. 33, 318-326.

Sydeman, W. J., García-Reyes, M., Schoeman, D. S., Rykaczewski, R. R., Thompson, S. A., Black, B. A., Bograd, S. J., 2014. Climate change and wind intensification in coastal upwelling ecosystems. Science. 345 (6192), 77-80.

Thomson, R. E., Krassovski, M. V., 2010. Poleward reach of the poleward undercurrent extension. J. Geophys. Res. 115, 1-9.

Torres, R., Barton, E. D, 2006. Onset and development of the Iberian Poleward Flow along the Galician coast. Cont. Shelf Res. 26, 1134-1153.

Ulloa, O., Pantoja, S. 2009. The oxygen minimum zone of the eastern South Pacific. Deep Sea Res. II. 56(16), 987-991.

Vargas, C., Martínez, R., San Martín, V., Aguayo, M., Silva, N., Torres, R., 2011. Allochthonous subsidies of organic matter across a lake–river–fjord landscape in the Chilean Patagonia: Implications for marine zooplankton in inner fjord areas. Cont. Shelf Res. 31, 187-201.

Yanicelli, B., Castro, L., Parada, C., Scheneider, W., Colas, F., Donoso, D., 2012. Distribution of Pleuroncodes monodon larvae over the continental shelf of south-central Chile: field and modeling evidence for partial local retention and transport. Prog. Oceanogr. 92–95, 206–227.

Wooster, W.S., Reid, J.L., 1963. Eastern boundary currents, in: Hill, M. (Ed.), The sea, Vol. 2, Wiley Interscience, New York, pp. 253–280.

Wooster, W.S., M. Gilmartin. 1961. The Peru-Chile Undercurrent. J. Mar. Res. 19 (3), 97-122.

Wyrtki, K., 1967. Circulation and water masses in the eastern equatorial Pacific Ocean. Int. J. Oceanol. Limnol. 1 (2), 117-147.

Figure 1: Simulated bathymetry of the study area.

Figure 2: Annual average of wind stress magnitude (N m^{-2}) (a) and wind stress curl 10^{-7} Nm^{-3} (b) derived from SCOW in the study zone.

Figure 3: Cross-shore profile of the alongshore average sea level anomaly in autumn (a,b) and spring (c,d). Taylor diagram of sea level anomaly for autumn, winter, spring and summer (e). Alongshore average of surface geostrophic velocity from the model (f).

Figure 4: Eddy Kinetic Energy (EKE): (a) ROMS and (b) AVISO.

Figure 5: Sea Surface Temperature: ROMS and Pathfinder, (a) Difference and (b) Hovmöller diagram in a 50-km wide coastal band.

Figure 6: Temperature and salinity cross-sections from ROMS simulation vs CARS data at 32ºS and 36ºS.

Figure 7: TS diagram at 35.5º-40°S; 72.75º-77.8°W (a) FIP data and (b) ROMS, TS diagram (c) north and (d) south boundary forcing and (e) percentage of water masses at 37ºS; 75.3ºW. FIP data (solid line) vs ROMS model (dashed line).

Figure 8: Current cross-sections at (a) 30ºS, (b) 33ºS, (c) 36ºS and (d) 39ºS

Figure 9: Mean wind stress intensity, N m^{-2} and mean wind stress curl, 10^{-7} N m^{-3} at 30º, 33º, 36º, and 39ºS in a cross section at 0 - 350 km offshore (a, b). Seasonal alongshore wind stress and seasonal wind stress curl, in a 300-km-wide coastal band (c, d).

Figure 10: (a) Mean current intensity (cm s^{-1}) and direction (arrows) between depths of 100-300 m and (b) Eddy kinetic energy (cm^2 s^{-2}) averaged between 200 and 300 m deep.

Figure 11: Longitudinal width and nucleus (black circles) of the PCUC at depth during autumn (Au), winter (Wi), spring (Sp), summer (Su) at 30°, 33°, 36° and 39°S. The black line indicates the continental shelf (ROMS) at 200 m depth.

Figure 12: Average monthly Sverdrup transport (Sv, poleward positive) of the PCUC at 30º, 33º, 36º and 39ºS.

Figure 13: Average deepening of maximum velocity nucleus of PCUC with Latitude (°S) by Leth et al. (2004), Shaffer et al. (1999) and this study.

Figure 14: Number of particles (in percent) that were launched seasonally in the PCUC at 33°S and upwelled (i.e. reached the 50m-deep surface layer) 6 months later in different latitude ranges. The mean time (in days) taken for the particles to upwell is also indicated.

Figure 15: Same as Figure 14 but for particles released at 37°S.

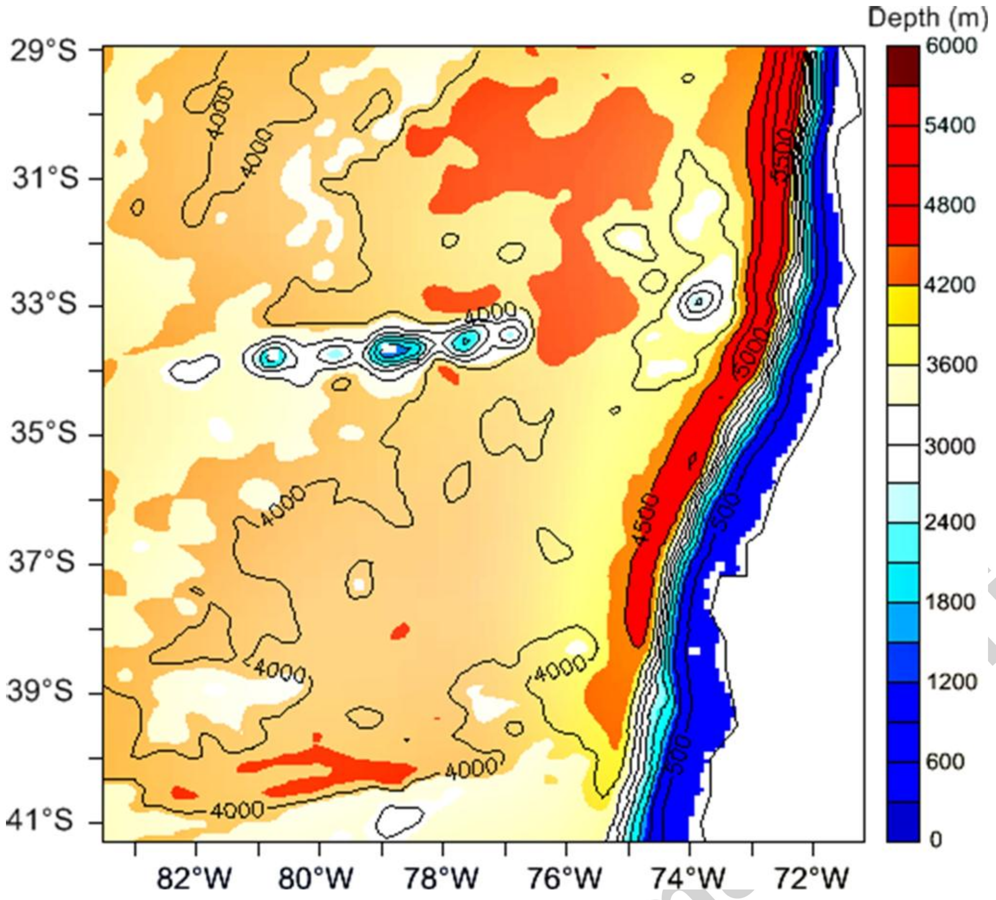
Depth (m)
6000
5400
4800
4200
3600
3000
2400
1800
1200
600
0
29°S
31°S
33°S
35°S
37°S
39°S
41°S
82°W
80°W
78°W
76°W
74°W
72°W
4000
4500
5000
500

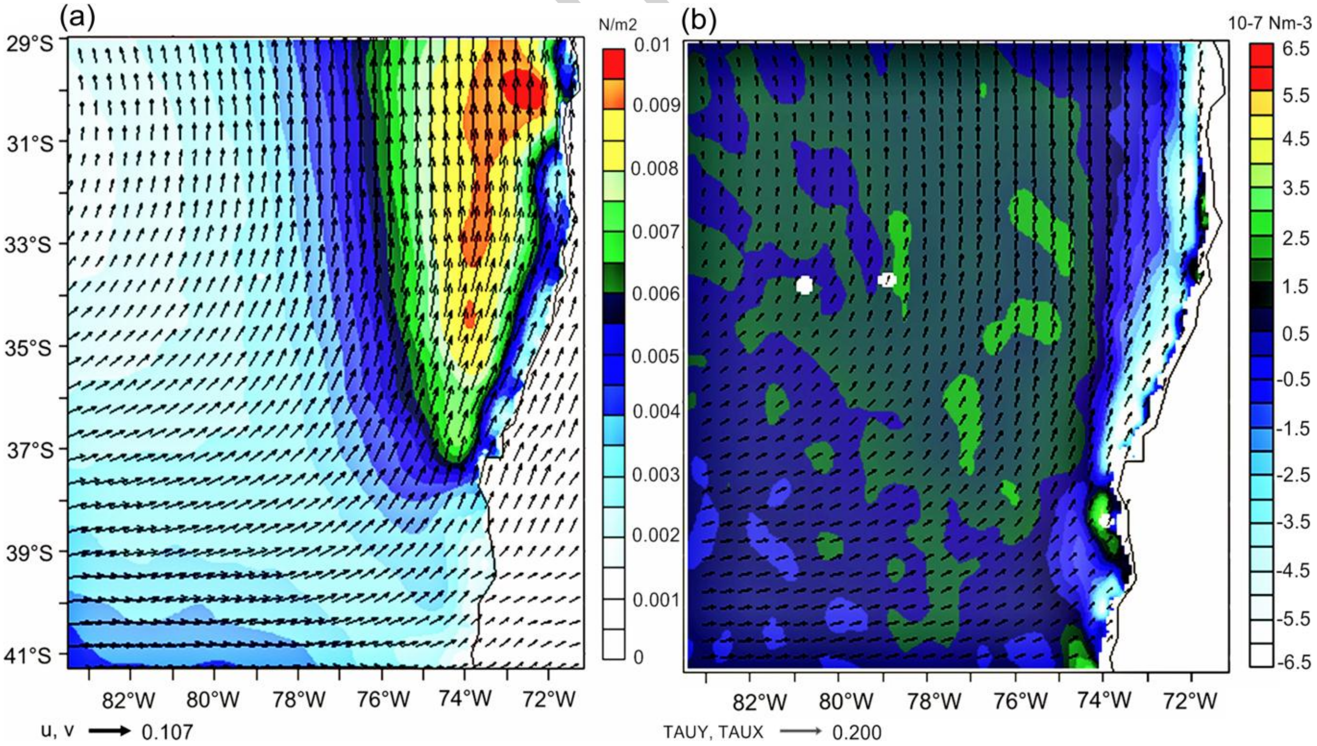
(a)
N/m2
0.01
0.009
0.008
0.007
0.006
0.005
0.004
0.003
0.002
0.001
0
29°S
31°S
33°S
35°S
37°S
39°S
41°S
82°W
80°W
78°W
76°W
74°W
72°W
u, v
0.107
(b)
10-7 Nm-3
6.5
5.5
4.5
3.5
2.5
1.5
0.5
-0.5
-1.5
-2.5
-3.5
-4.5
-5.5
-6.5
TAUY, TAUX
0.200

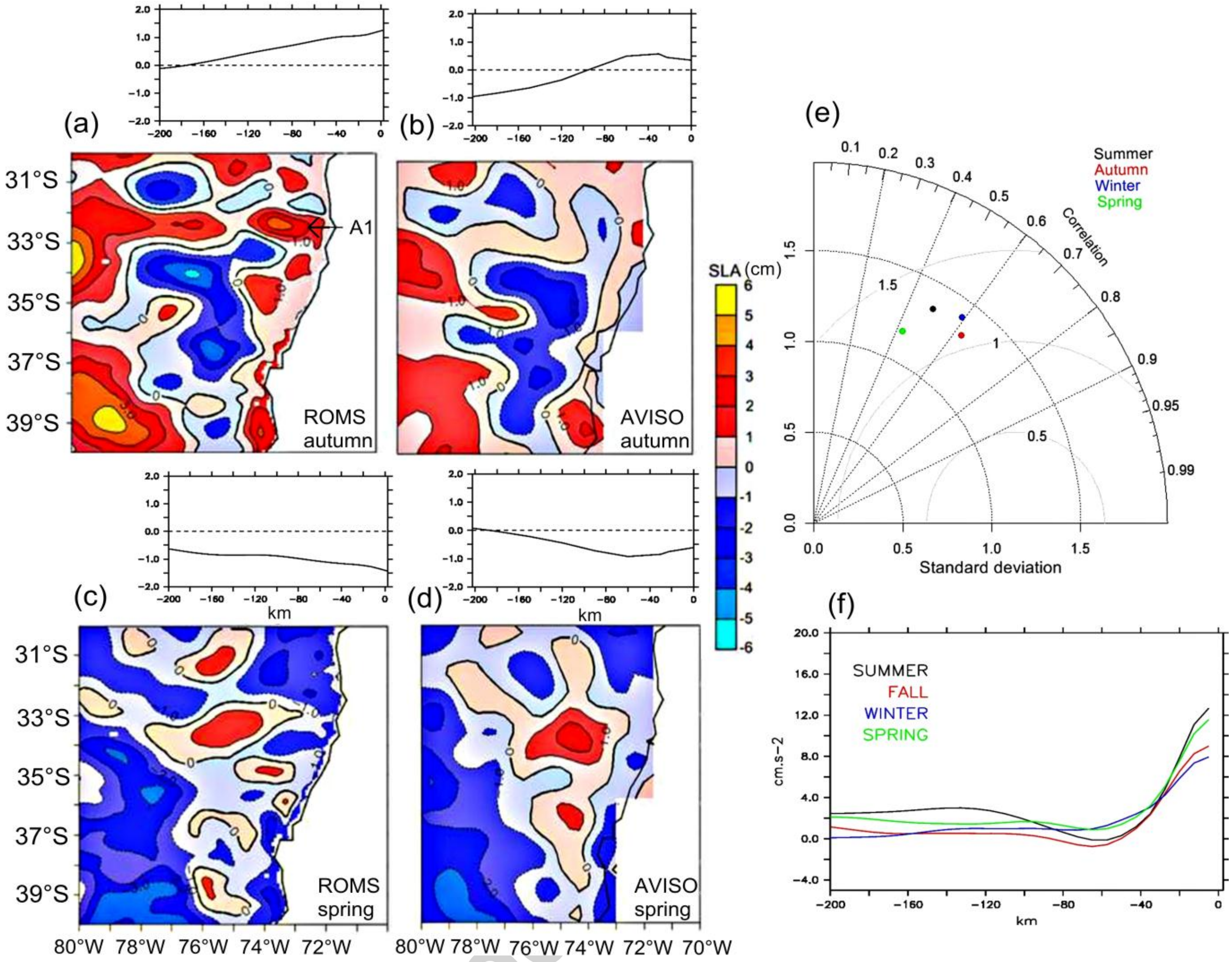
(a)
(b)
(c)
(d)
(e)
(f)
31°S
33°S
35°S
37°S
39°S
A1
ROMS autumn
AVISO autumn
ROMS spring
AVISO spring
SLA (cm)
6
5
4
3
2
1
0
-1
-2
-3
-4
-5
-6
km
80°W 78°W 76°W 74°W 72°W 70°W
Summer
Autumn
Winter
Spring
Correlation
Standard deviation
SUMMER
FALL
WINTER
SPRING
cm.s−2

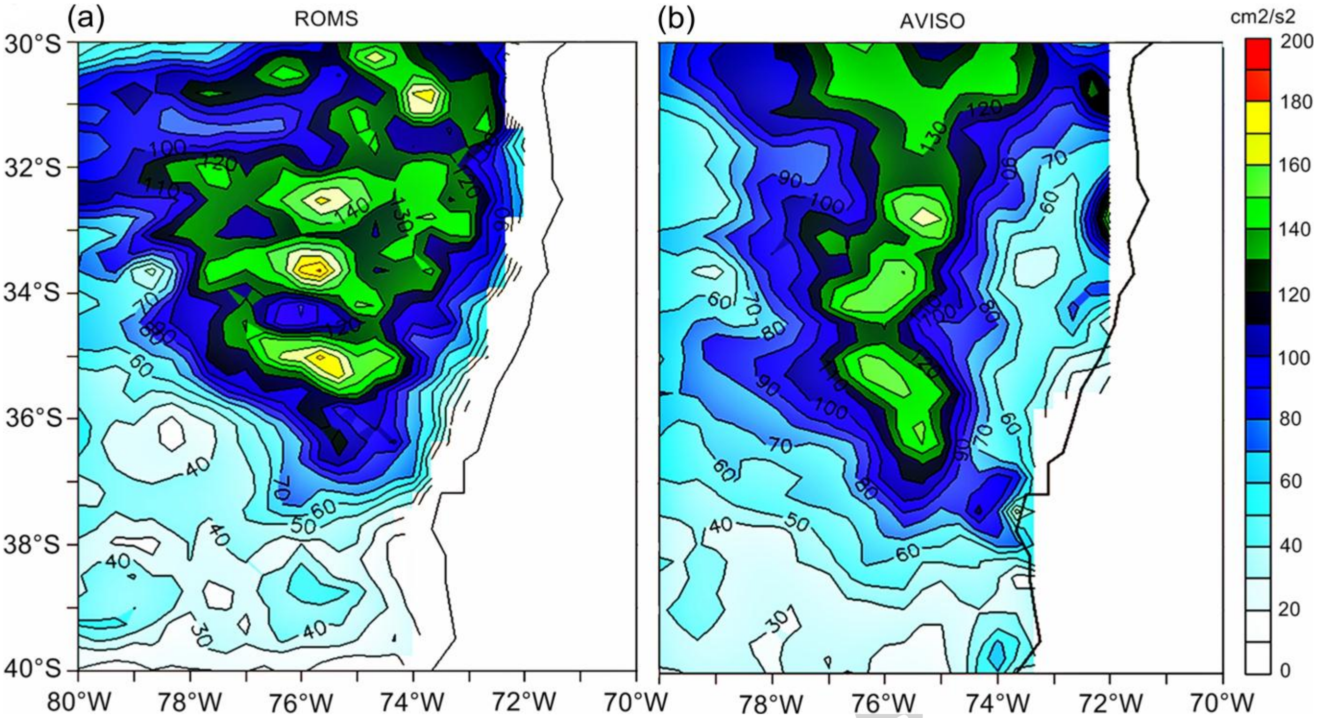
(a)
ROMS
(b)
AVISO
cm2/s2
30°S
32°S
34°S
36°S
38°S
40°S
80°W
78°W
76°W
74°W
72°W
70°W
0
20
40
60
80
100
120
140
160
180
200

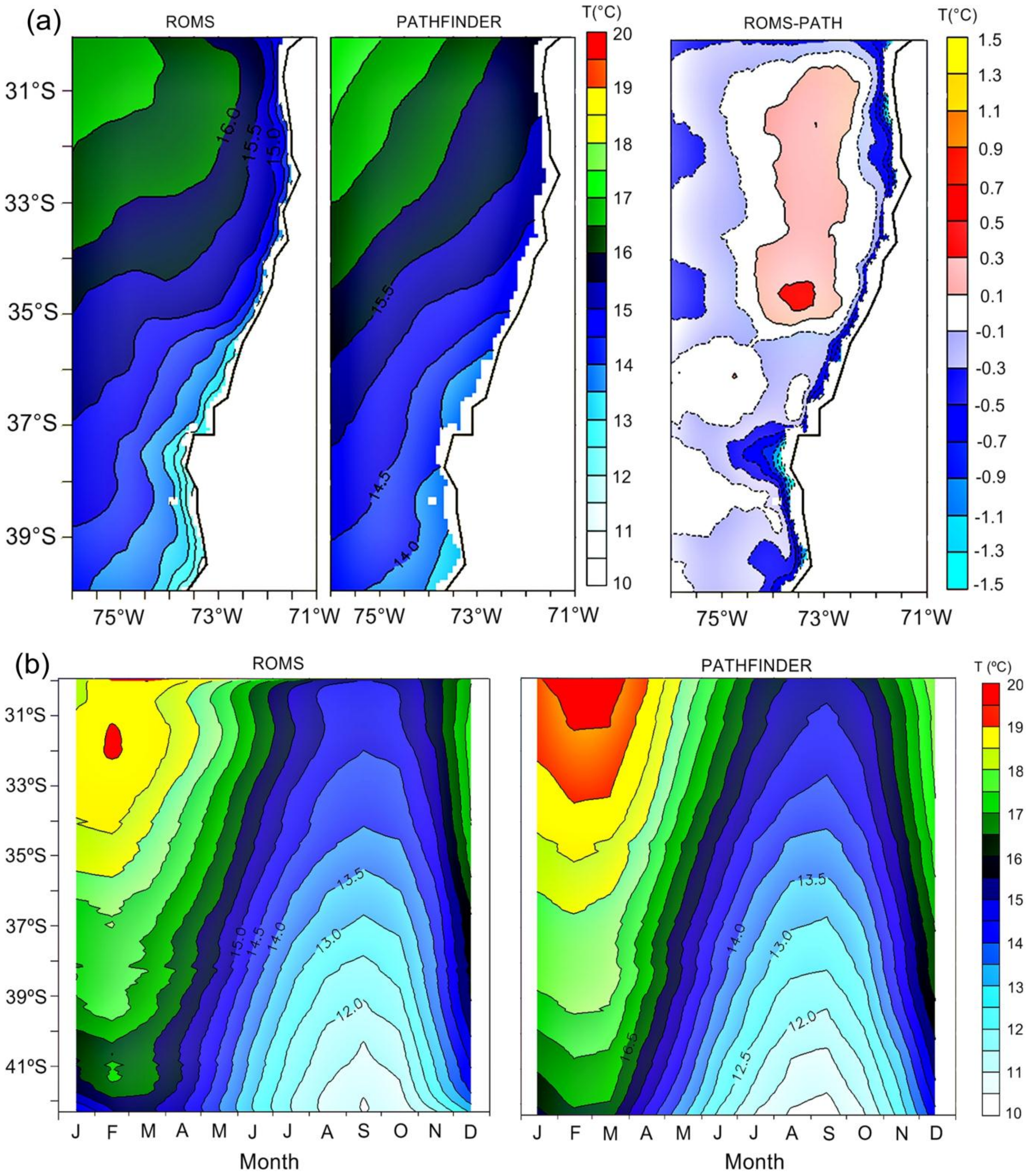
(a)
ROMS
PATHFINDER
ROMS-PATH
T(°C)
20
19
18
17
16
15
14
13
12
11
10
T(°C)
1.5
1.3
1.1
0.9
0.7
0.5
0.3
0.1
-0.1
-0.3
-0.5
-0.7
-0.9
-1.1
-1.3
-1.5
31°S
33°S
35°S
37°S
39°S
75°W
73°W
71°W
16.0
15.5
15.0
14.5
14.0
(b)
ROMS
PATHFINDER
T (ºC)
31ºS
33ºS
35ºS
37ºS
39ºS
41ºS
J
F
M
A
M
J
J
A
S
O
N
D
Month
13.5
13.0
12.0
12.5
16.5

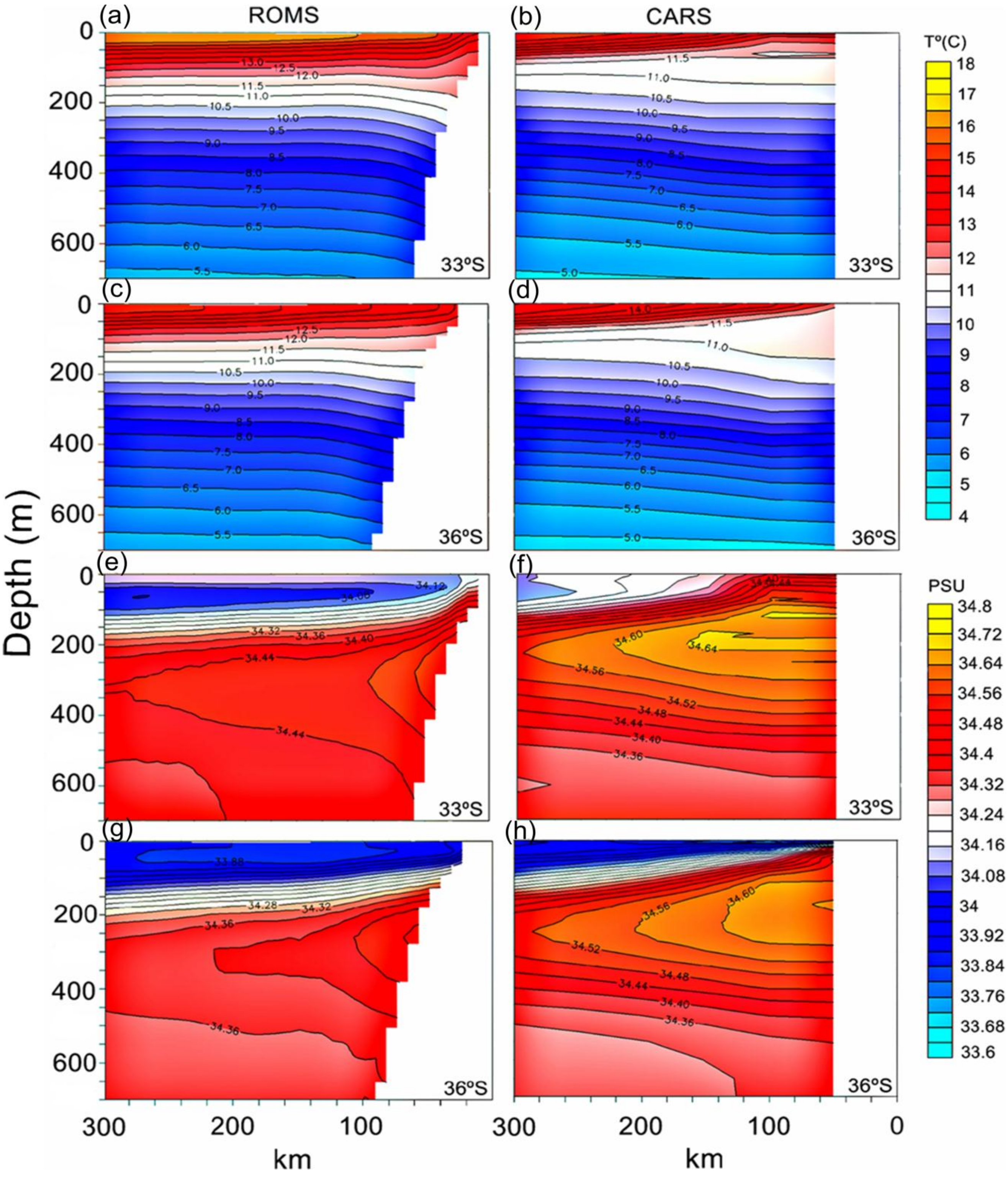
(a)
ROMS
(b)
CARS
(c)
(d)
(e)
(f)
(g)
(h)
33ºS
36ºS
Depth (m)
km
0
200
400
600
300
200
100
0
Tº(C)
18
17
16
15
14
13
12
11
10
9
8
7
6
5
4
PSU
34.8
34.72
34.64
34.56
34.48
34.4
34.32
34.24
34.16
34.08
34
33.92
33.84
33.76
33.68
33.6

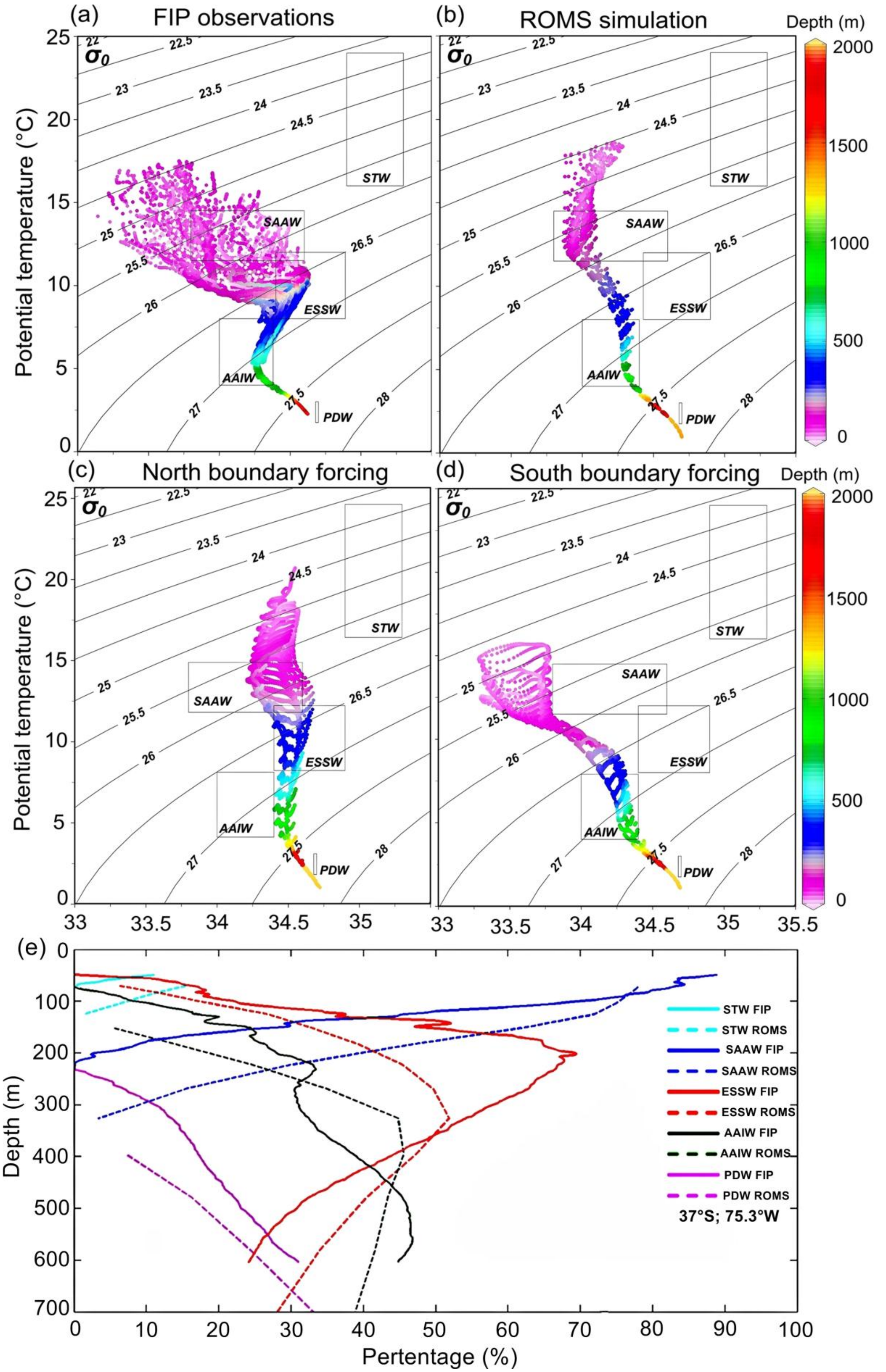
(a) FIP observations
(b) ROMS simulation
(c) North boundary forcing
(d) South boundary forcing
(e)
Potential temperature (°C)
Depth (m)
σ0
STW
SAAW
ESSW
AAIW
PDW
22
22.5
23
23.5
24
24.5
25
25.5
26
26.5
27
27.5
28
0
500
1000
1500
2000
33
33.5
34
34.5
35
35.5
0
100
200
300
400
500
600
700
10
20
30
40
50
60
70
80
90
100
Pertentage (%)
STW FIP
STW ROMS
SAAW FIP
SAAW ROMS
ESSW FIP
ESSW ROMS
AAIW FIP
AAIW ROMS
PDW FIP
PDW ROMS
37°S; 75.3°W

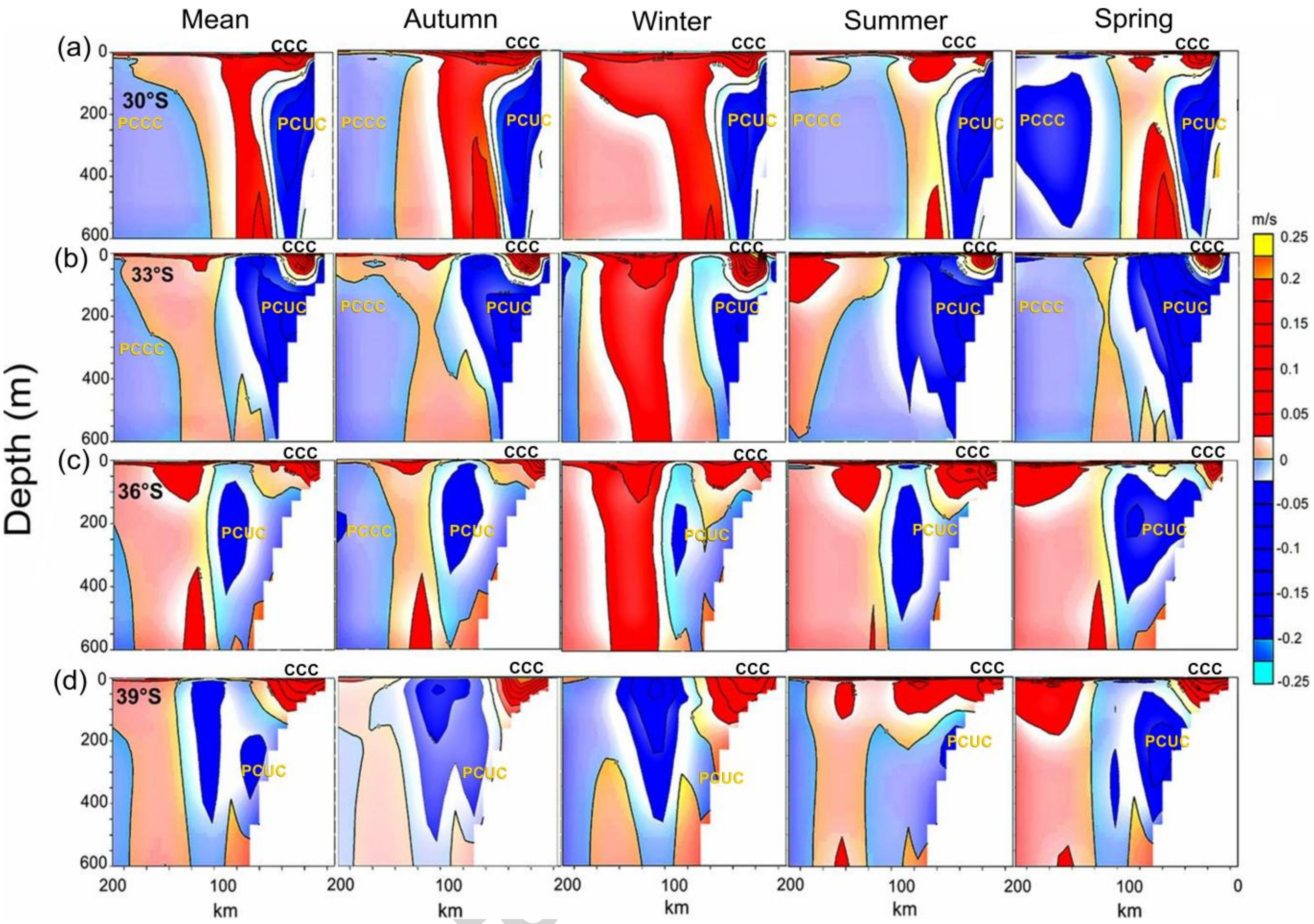
Mean
Autumn
Winter
Summer
Spring
(a)
(b)
(c)
(d)
30°S
33°S
36°S
39°S
CCC
PCCC
PCUC
Depth (m)
0
200
400
600
km
200
100
0
m/s
0.25
0.2
0.15
0.1
0.05
0
-0.05
-0.1
-0.15
-0.2
-0.25

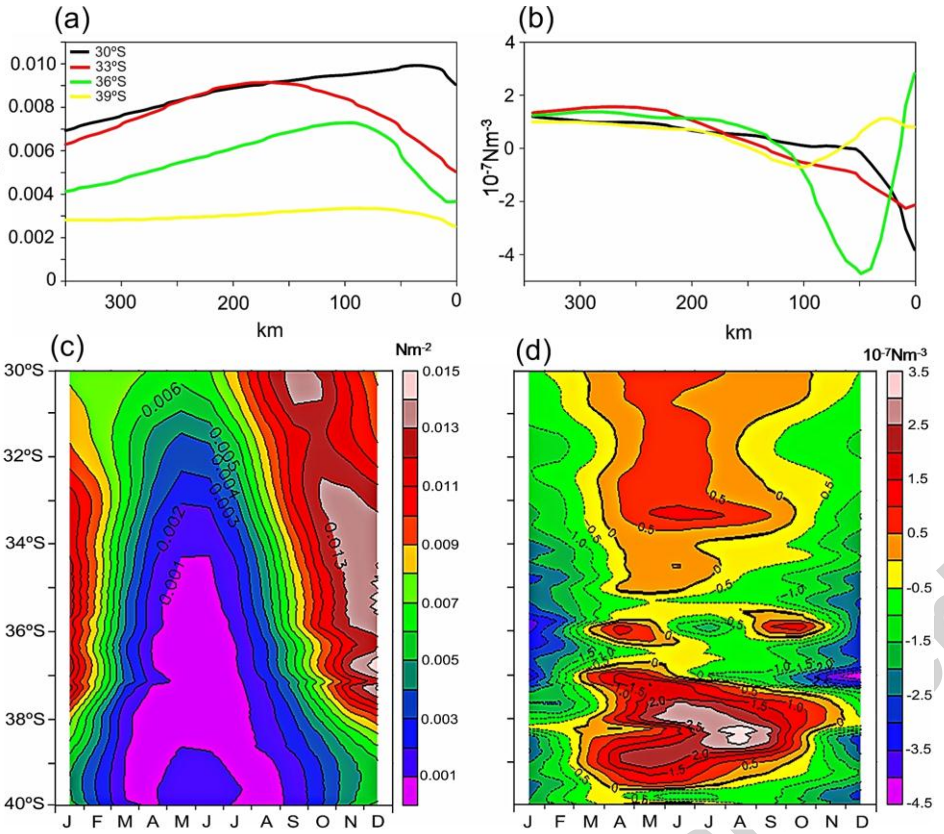
(a)
30ºS
33ºS
36ºS
39ºS
Nm-2
0.010
0.008
0.006
0.004
0.002
0
300
200
100
0
km
(b)
10^{-7}Nm^{-3}
4
2
0
-2
-4
300
200
100
0
km
(c)
Nm-2
30ºS
32ºS
34ºS
36ºS
38ºS
40ºS
J F M A M J J A S O N D
0.015
0.013
0.011
0.009
0.007
0.005
0.003
0.001
0.006
0.005
0.004
0.003
0.002
0.001
0.013
(d)
10^{-7}Nm^{-3}
3.5
2.5
1.5
0.5
-0.5
-1.5
-2.5
-3.5
-4.5
J F M A M J J A S O N D
0.5
0
-0.5
-1.0
-1.5
1.0
1.5
2.0
2.5
-2.0

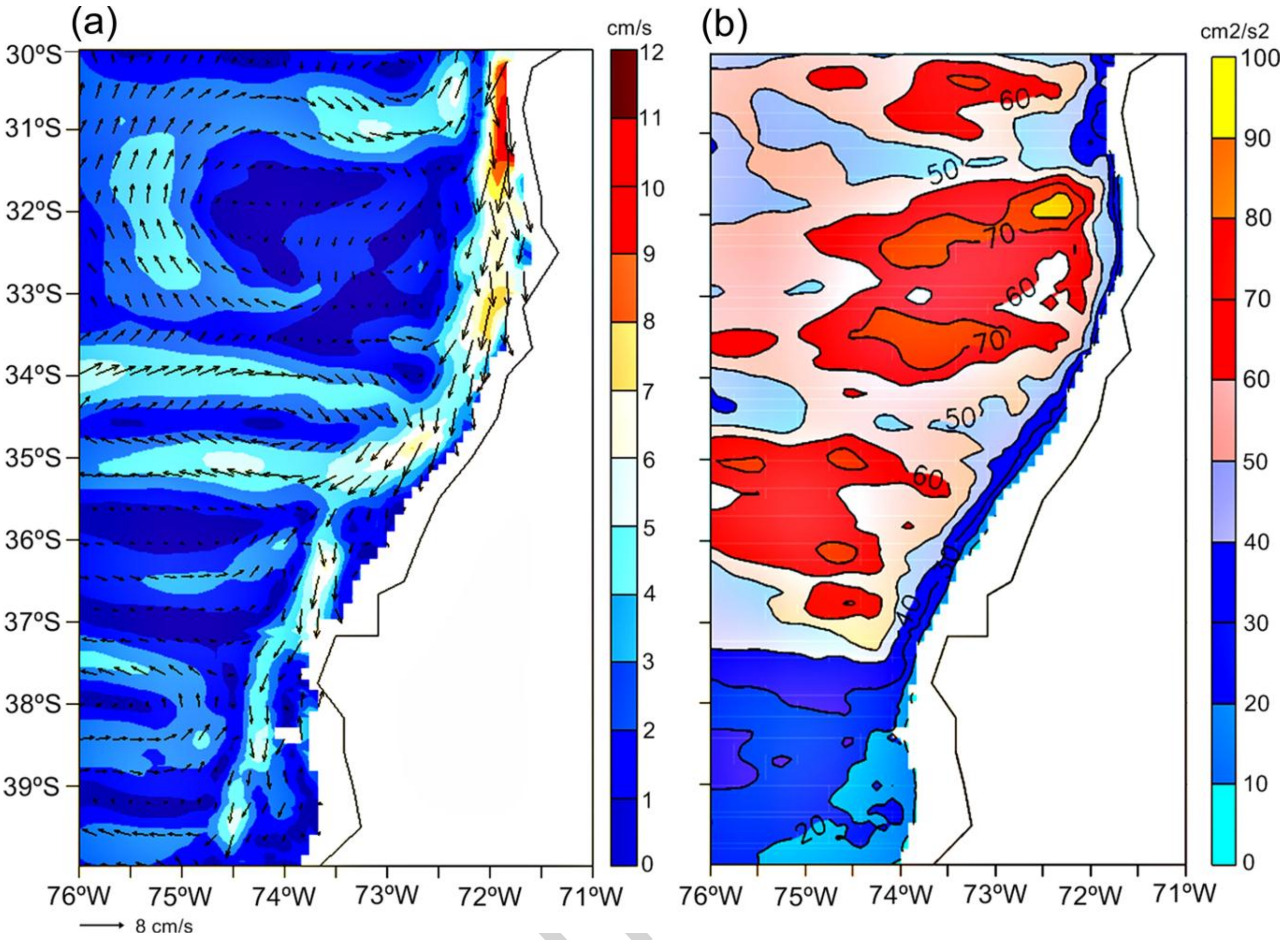
(a)
cm/s
30ºS
31ºS
32ºS
33ºS
34ºS
35ºS
36ºS
37ºS
38ºS
39ºS
76ºW
75ºW
74ºW
73ºW
72ºW
71ºW
8 cm/s
0
1
2
3
4
5
6
7
8
9
10
11
12
(b)
cm2/s2
60
50
70
60
70
50
60
50
40
20
0
10
20
30
40
50
60
70
80
90
100

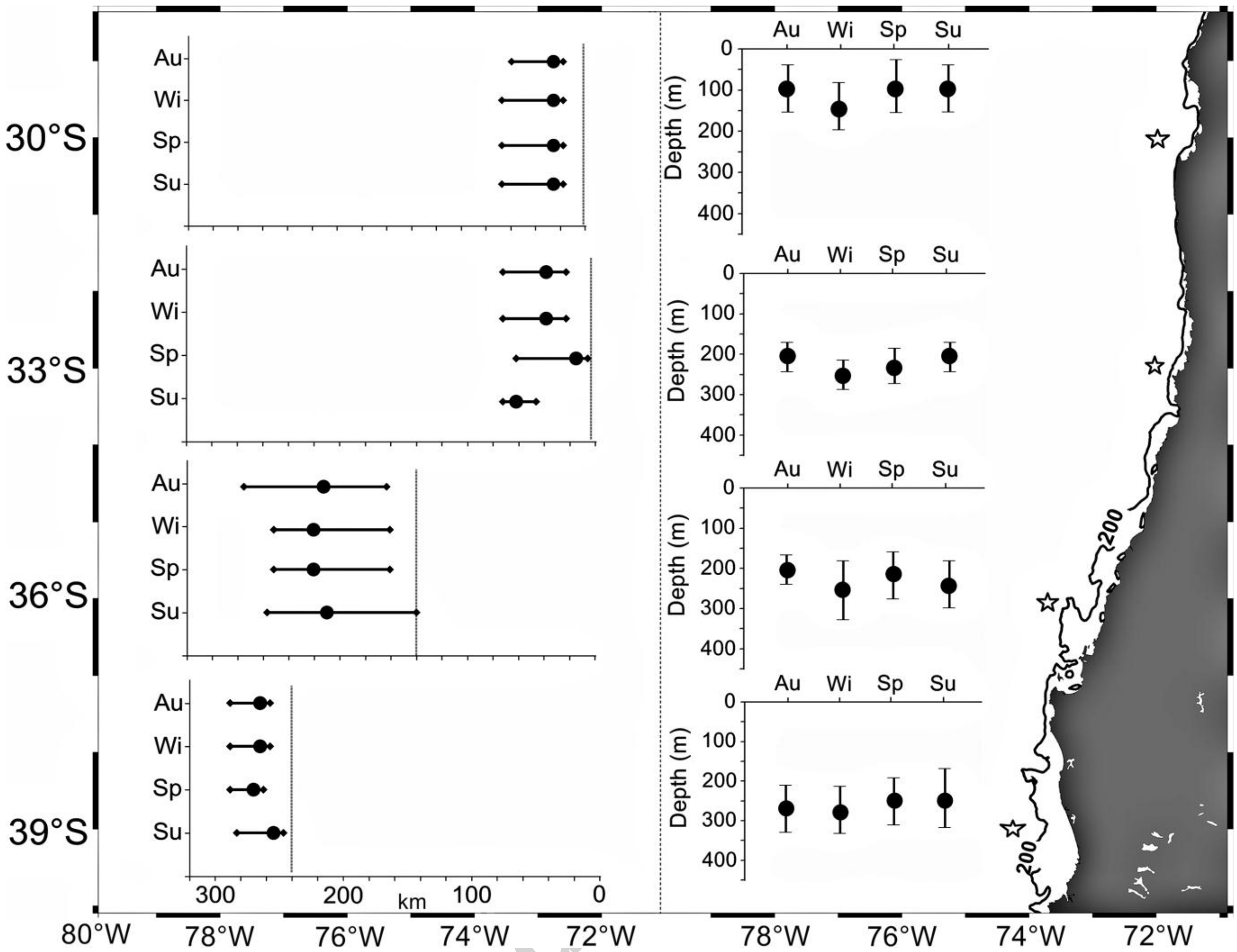
30°S
33°S
36°S
39°S
Au
Wi
Sp
Su
300
200
km
100
0
Depth (m)
0
100
200
300
400
200
80°W
78°W
76°W
74°W
72°W
78°W
76°W
74°W
72°W

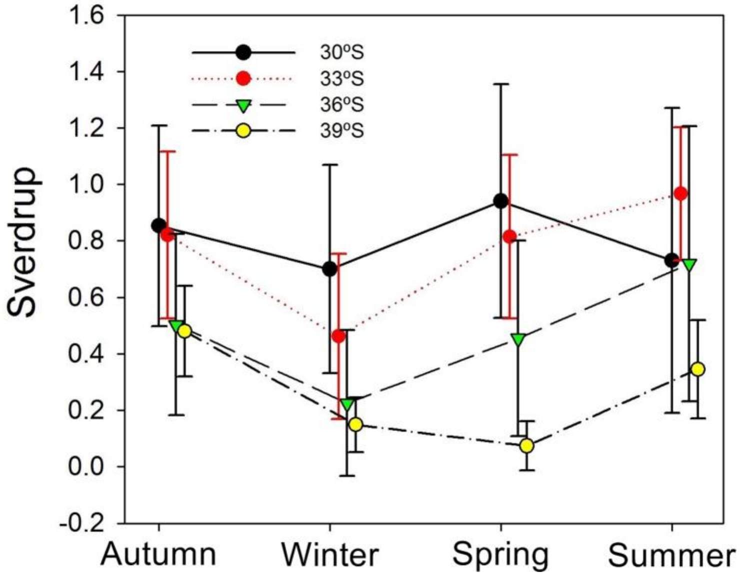
Sverdrup
1.6
1.4
1.2
1.0
0.8
0.6
0.4
0.2
0.0
-0.2
30ºS
33ºS
36ºS
39ºS
Autumn
Winter
Spring
Summer

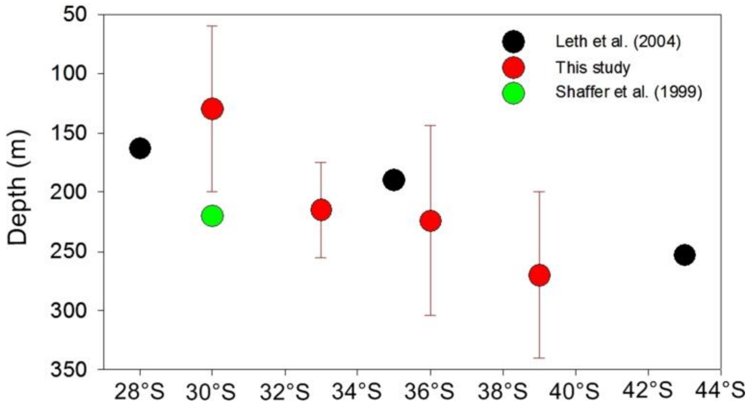
Leth et al. (2004)
This study
Shaffer et al. (1999)
Depth (m)
50
100
150
200
250
300
350
28°S
30°S
32°S
34°S
36°S
38°S
40°S
42°S
44°S

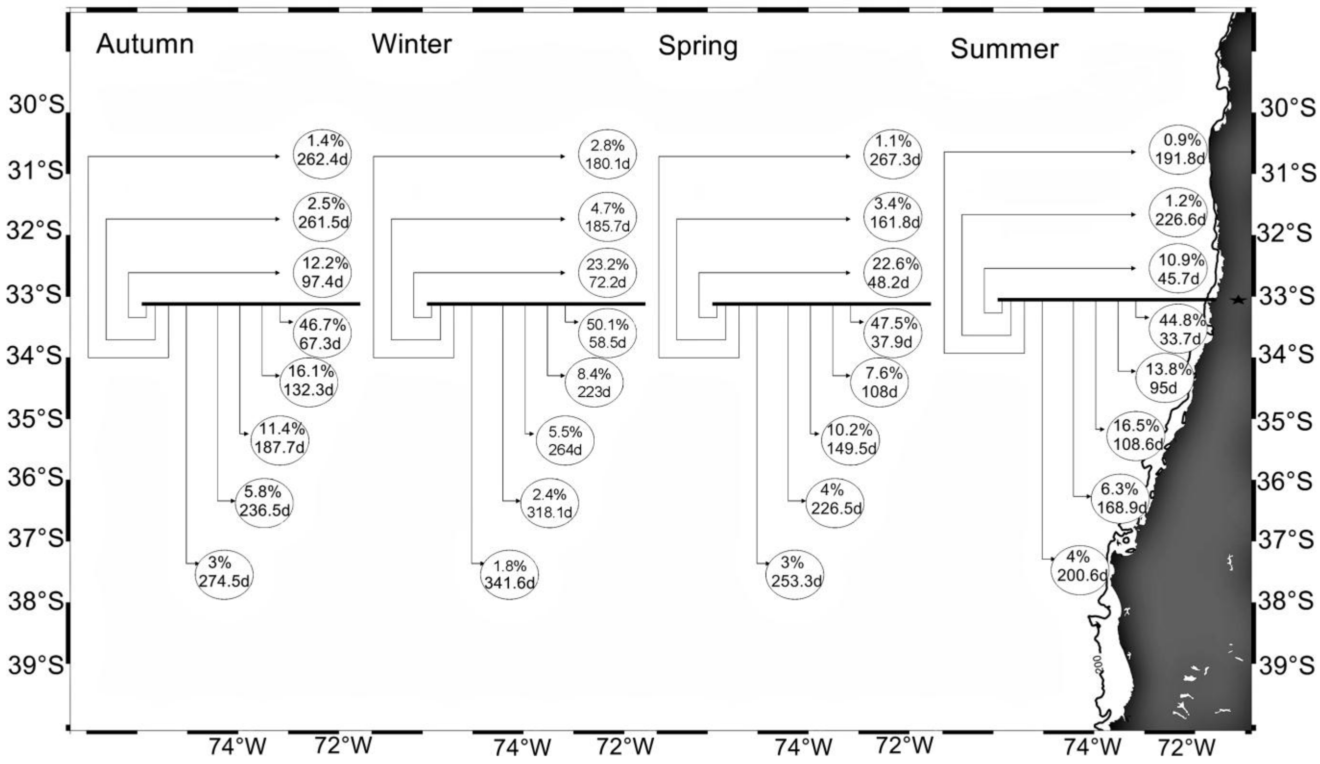
Autumn
Winter
Spring
Summer
30°S
31°S
32°S
33°S
34°S
35°S
36°S
37°S
38°S
39°S
1.4% 262.4d
2.5% 261.5d
12.2% 97.4d
46.7% 67.3d
16.1% 132.3d
11.4% 187.7d
5.8% 236.5d
3% 274.5d
2.8% 180.1d
4.7% 185.7d
23.2% 72.2d
50.1% 58.5d
8.4% 223d
5.5% 264d
2.4% 318.1d
1.8% 341.6d
1.1% 267.3d
3.4% 161.8d
22.6% 48.2d
47.5% 37.9d
7.6% 108d
10.2% 149.5d
4% 226.5d
3% 253.3d
0.9% 191.8d
1.2% 226.6d
10.9% 45.7d
44.8% 33.7d
13.8% 95d
16.5% 108.6d
6.3% 168.9d
4% 200.6d
200
74°W
72°W
74°W
72°W
74°W
72°W
74°W
72°W

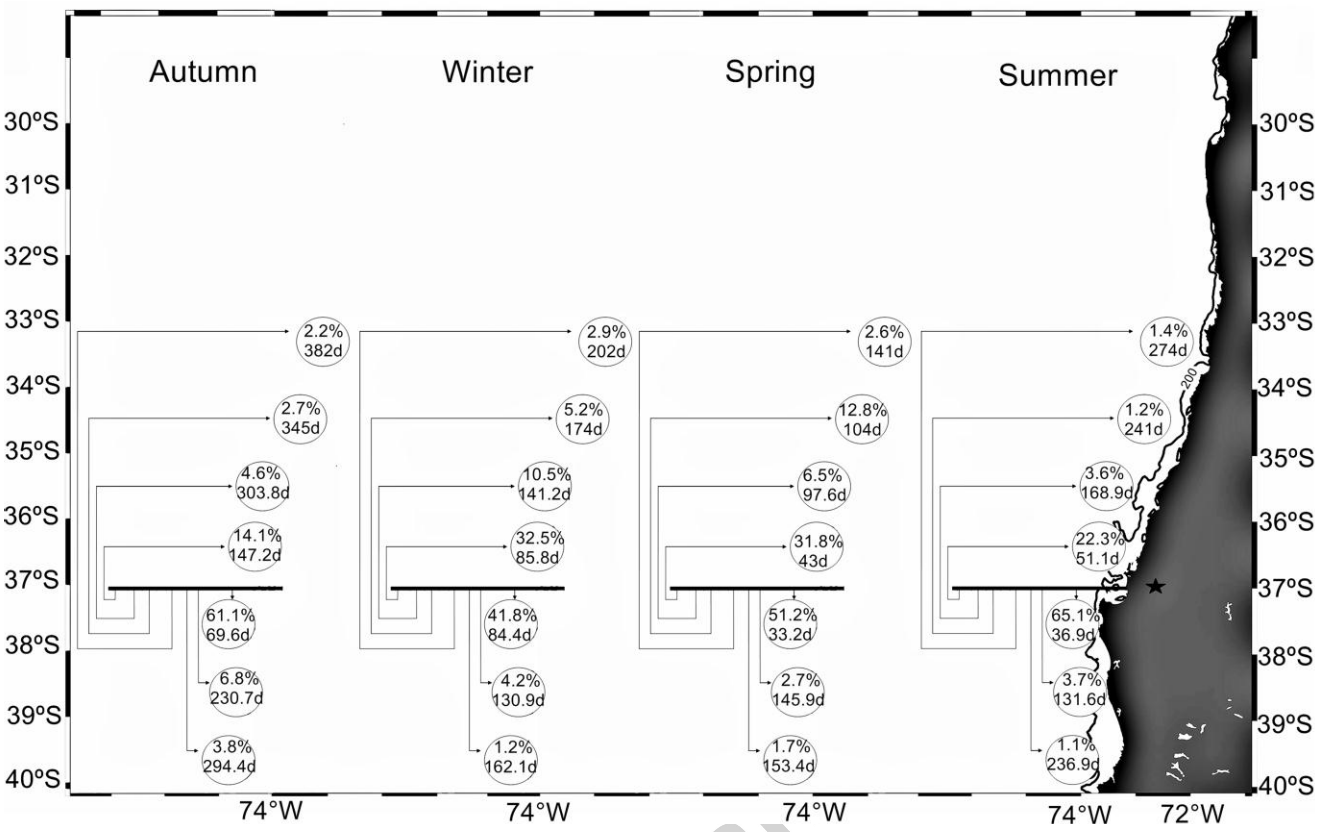

Table I: Seasonal and annual mean poleward transport (in Sv, positive poleward) of the Peru-Chile Undercurrent at 30°S, 33ºS, 36ºS and 39°S. The transport was calculated from model output in our study and Aguirre et al. (2012), and from observations in Leth et al. (2004) and Shaffer et al. (1997,1999). Variability corresponding to the standard deviation around the mean for the 9-year simulation is indicated.

Latitude/ Season	***This study***	***Aguirre et al. (2012)***	***Leth et al. (2004)***	***Shaffer et al. (1997, 1999)***
28°S			1.3	
30°S				
Fall	0.85 ± 0.36	1.06		
Winter	0.68 ± 0.37	0.86		
Spring	0.94 ± 0.41	0.87		
Summer	0.73 ± 0.54	0.81		
Average	0.80 ± 0.4	0.9		1
33°S				
Fall	0.82 ± 0.23	0.81		
Winter	0.46 ± 0.29	0.61		
Spring	0.81 ± 0.29	0.7		
Summer	0.90 ± 0.24	0.73		

Average	0.76 ± 0.17	0.71	
35°S			
Average	0.76 ± 0.36		1.3
36°S			
Fall	0.50 ± 0.32	0.68	
Winter	0.22 ± 0.26	0.55	
Spring	0.45 ± 0.35	0.43	
Summer	0.71 ± 0.49	0.85	
Average	0.47 ± 0.17	0.62	
39°S			
Fall	0.48 ± 0.16	0.34	
Winter	0.15 ± 0.10	0.20	
Spring	0.08 ± 0.09	-	
Summer	0.34 ± 0.17	0.17	
Average	0.26 ± 0.09	0.27 ± 0.09	
43°S			1.1

Table II: Percentage/initial depth of floats that upwell in the surface layer (50m depth) with respect to the total number of floats launched in the PCUC at 33°S and 37°S, for each season. Standard deviations indicate interannual variability due to the impact of mesoscale turbulence, which differs from year to year.

Percentage / initial depth of upwelled floats		
Season	***33°S***	***37°S***
Autumn	19.6 ± 4.6/110 ± 28	13.9 ± 4.5/108 ± 16
Winter	20.2 ± 7.1/131 ± 42	16.5 ± 5.9/102 ± 20
Spring	19.2 ± 4.5/120 ± 38	12.8 ± 4.9/119 ± 56
Summer	19.3 ± 3.7/107 ± 30	16 ± 4.9/116 ± 22

Table III: Statistics (mean and standard deviation) of the positions (latitude, depth and distance to the coast) of the floats that had not upwelled 6 months after being launched from the 33°S and 37°S sections.

Latitude of launch	***Season***	***Latitude (ºS)***	***Distance to coast (km)***	***Depth (m)***
33ºS	Winter	33.0 ± 1.5	294 ± 157	322 ± 167
37ºS	Winter	36.2 ± 1.5	330 ± 202	340 ± 174
33ºS	Summer	34.5 ± 2.0	284 ± 198	327 ± 169
37ºS	Summer	37.3 ± 1.7	263 ± 153	361 ± 184

Table IV: Meridional transport (in Sv, positive poleward) between 0 and 650m at different latitudes, and

Sverdrup transport (in Sv, positive poleward) in a coastal band of 50 to 100 km from the coast.

Transport	*Distance*	*30ºS*	*33ºS*	*36ºS*	*39ºS*
Model	50 km band	1.03±1.08	-0.54±1.2	0.31±0.69	0.79±0.46
Model	100 km band	1.65±1.60	-1.07±1.3	0.49±1.2	1.19±0.7
Sverdrup	50 km band	1.39	0.20	0.40	0.29
Sverdrup	100 km band	1.48	0.64	1.1	0.32

Highlights

- We analysed the Peru-Chile Undercurrent using a ROMS model
- The results were validated using observations from the Eastern South Pacific Region
- Poleward decrease in wind stress curl reduces PCUC strength
- There is a deepening of the maximum velocity nucleus of the Peru-Chile Undercurrent
- Less than 20% of the particles transported by the undercurrent upwell after 6 months